J. Fluid Mech. (1999), *vol.* 393, *pp.* 23–57. Printed in the United Kingdom

Numerical and experimental investigations of oblique boundary layer transition

By STELLAN BERLIN[1], MARKUS WIEGEL[2] AND DAN S. HENNINGSON[3]

[1]Department of Mechanics, KTH, S-10044 Stockholm, Sweden
[2]Institut für Strömungsmechanik, Bunsenstraße 10, D-37073 Göttingen, Germany
[3]FFA, Box 11021, S-16111 Bromma, Sweden

(Received 5 January 1998 and in revised form 20 January 1999)

A transition scenario initiated by two oblique waves is studied in an incompressible boundary layer. Hot-wire measurements and flow visualizations from the first boundary layer experiment on this scenario are reported. The experimental results are compared with spatial direct numerical simulations and good qualitative agreement is found. Also, quantitative agreement is found when the experimental device for disturbance generation is closely modelled in the simulations and pressure gradient effects taken into account. The oblique waves are found to interact nonlinearly to force streamwise vortices. The vortices in turn produce growing streamwise streaks by non-modal linear growth mechanisms. This has previously been observed in channel flows and calculations of both compressible and incompressible boundary layers. The flow structures observed at the late stage of oblique transition have many similarities to the corresponding ones of K- and H-type transition, for which two-dimensional Tollmien–Schlichting waves are the starting point. However, two-dimensional Tollmien–Schlichting waves are usually not initiated or observed in oblique transition and consequently the similarities are due to the oblique waves and streamwise streaks appearing in all three scenarios.

1. Introduction

1.1. *Tollmien–Schlichting waves*

Transition from laminar to turbulent flow in viscous boundary layers is of great practical interest and is far from understood. One possible route to transition that has been observed in low-noise environments starts with the secondary instability of unstable Tollmien–Schlichting (TS) waves. The majority of the research efforts on laminar–turbulent transition has been focused on this scenario. Its first stage, or primary instability, is the growth of two-dimensional TS-waves and can be predicted by solving the Orr–Sommerfeld equation for exponential instabilities. The two-dimensional state has been found to develop into one of two three-dimensional states, then to turbulence. Herbert (1983*a*,*b*) found that the two three-dimensional states were caused by secondary instabilities of the two-dimensional state. These occur if the amplitude of the two-dimensional TS-wave is above a given threshold. One of the three-dimensional states was observed experimentally by Klebanoff, Tidstrom & Sargent (1962) and is called K-type or fundamental breakdown. The other was first observed by Kachanov, Kozlov & Levchenko (1977) and goes under the names

H-type or subharmonic breakdown. Kachanov (1994) calls it N-type transition in his review of the physical mechanisms involved in transition. A review of the theoretical efforts concerning the secondary instabilities has been written by Herbert (1988). Kleiser & Zang (1991) have reviewed the numerical work in the area. Details of these scenarios are presented in § 4, where the results on oblique transition presented here are discussed in the light of previous findings.

1.2. *Non-modal growth*

Before the 1940s experimental investigators were unable to identify TS-waves and the subsequent secondary instability in either boundary layers or channel flows. Transition was instead thought to be caused by other disturbances and other growth mechanisms. These are obviously as likely now as they were then. Morkovin (1969) stated 'We can bypass the TS-mechanism altogether', and transition caused by growth mechanisms other than exponential instabilities is often denoted *bypass-transition.* The growth mechanisms behind bypass transition can be found by examining the linearized Navier–Stokes equations. Since the nonlinear terms are conservative in the Navier–Stokes equations they cannot by themselves be responsible for production of disturbance energy. In fact, considering the evolution equation for the total disturbance energy, the so called Reynolds–Orr equation, all of the nonlinear terms drop out, implying that the instantaneous growth rate is independent of the disturbance energy (see e.g. Joseph 1976; Henningson 1996).

The existence of growth mechanisms other than those associated with exponential growth were known already to Orr (1907) and Kelvin (1887), but the investigations by Gustavsson (1991), Butler & Farell (1992), Reddy & Henningson (1993), Trefethen *et al.* (1993) showing the possible magnitude of non-modal growth, clearly indicated their potential for causing transition.

In order to briefly discuss the concept of non-modal transient growth and relate it to the mathematical characteristics of the governing equations we will consider the linear disturbance equations Fourier transformed in the wall-parallel directions. We have

$$\frac{\mathrm{d}\hat{\boldsymbol{u}}}{\mathrm{d}t} = \mathscr{L}\hat{\boldsymbol{u}}(t), \quad \hat{\boldsymbol{u}}(0) = \hat{\boldsymbol{u}}_0, \tag{1.1}$$

where $\mathscr{L}$ is the linearized Navier–Stokes operator around a parallel mean flow and $\hat{\boldsymbol{u}}$ the Fourier-transformed disturbance flow vector $\boldsymbol{u}$. The solution can be written $\hat{\boldsymbol{u}}(t) = \exp(t\mathscr{L})\hat{\boldsymbol{u}}_0$ and the maximum growth experienced at time t as

$$\max_{\hat{\boldsymbol{u}}_0} \frac{\|\hat{\boldsymbol{u}}(t)\|}{\|\hat{\boldsymbol{u}}_0\|} = \| \exp(t\mathscr{L}) \| . \tag{1.2}$$

The norm is here taken as the disturbance energy integrated over the wall-normal direction

$$\| \hat{\boldsymbol{u}}(t) \| = \left(\int |\hat{\boldsymbol{u}}(y,t)|^2 \mathrm{d}y \right)^{1/2} . \tag{1.3}$$

It is possible to obtain a bound on the maximum growth of the following form:

$$\exp(\mathrm{Re}\{\lambda_{max}\}) \leqslant \| \exp(t\mathscr{L}) \| \leqslant \kappa \exp(\mathrm{Re}\{\lambda_{max}\}). \tag{1.4}$$

The constant κ can be thought of as the condition number of the 'matrix of eigenvectors', a concept that can be generalized to infinite-dimensional operators (Trefethen

1997). If $\mathscr{L}$ were a normal operator or equivalently if all of its eigenfunctions were orthogonal, this condition number would be unity, i.e. $\kappa = 1$. For streamwise-independent disturbances or streaks, which experience the largest non-modal growth, it can be shown that $\kappa = O(R)$ (S. C. Reddy, private communication), where R is the Reynolds number based on a suitable boundary layer thickness. The physical mechanism behind this growth is the *lift-up* effect (Landahl 1975). Weak streamwise counter-rotating vortices in the shear layer can lift up fluid with low streamwise velocity from the wall and bring high-speed fluid down towards the wall. This will create streaks of large amplitude in the streamwise velocity component. In the inviscid case the corresponding perturbation amplitude grows linearly with time, something recognized by Ellingsen & Palm (1975).

Another consequence of a non-normal operator is that the corresponding linear system may show a large response to forcing, although the forcing is not at a resonance condition. Let us consider the linear problem above, driven by a real frequency ω and an arbitrary forcing function $\hat{\boldsymbol{v}}$

$$\frac{\mathrm{d}\hat{\boldsymbol{u}}}{\mathrm{d}t} = \mathscr{L}\hat{\boldsymbol{u}}(t) + \mathrm{e}^{\mathrm{i}\omega t}\hat{\boldsymbol{v}}(x, y, z); \tag{1.5}$$

the time asymptotic response is given by

$$\hat{u}(t) = \mathrm{e}^{\mathrm{i}\omega t}(\mathrm{i}\omega I - \mathscr{L})^{-1}\hat{\boldsymbol{v}}. \tag{1.6}$$

The response is given by the resolvent $(\mathrm{i}\omega I - \mathscr{L})^{-1}$, which can be given the following bound:

$$\frac{1}{|\lambda - \mathrm{i}\omega|} \leqslant \|(\mathrm{i}\omega I - \mathscr{L})^{-1}\| \leqslant \frac{\kappa}{|\lambda - \mathrm{i}\omega|}, \tag{1.7}$$

where $|\lambda - \mathrm{i}\omega|$ represents the closest distance between $\mathrm{i}\omega$ and the spectrum of $\mathscr{L}$ (Trefethen 1993; Kreiss, Lundbladh & Henningson 1994). For streamwise-independent disturbances the distance between ω and the closest eigenvalue to $\mathscr{L}$ is $O(1/R)$, which together with the size of the condition number κ implies that the response is bounded by $O(R^2)$. A summary of results on optimal transient growth and optimal forcing, from several shear flows, is found in table 1.

In most of the theoretical work on non-modal growth a temporal formulation has been used. The disturbances are then thought to grow in time, which simplifies analysis and calculations. In a physical experiment or a spatial simulation, however, disturbances grow in space. Recently non-modal growth in boundary layers has been considered in spatial formulations by Luchini (1996) and Andersson, Berggren & Henningson (1997, 1999). They found in their analyses that the maximum possible energy growth scales linearly with the distance from the leading edge.

The possibilities of strong growth discussed above suggest that transition can occur even when no exponential instabilities exist. In cases where exponential instabilities are present, there will be a competition between or combination of the different mechanisms depending on the disturbances present. And obviously the nonlinear coupling between different disturbances will play an important role, as well. The non-modal growth of streamwise streaks is just the first step of transition. The possibility of a subsequent secondary instability of streaks and growth of three-dimensional disturbances has been investigated by Reddy *et al.* (1998) for channel flows. They found that streak breakdown is caused by an inflectional secondary

Flow	Quantity	Value	α	β
Couette	max resonance $\sup_{\omega\in\mathbb{R}} \|(\omega I - \mathscr{L})^{-1}\|$	$(R/8.12)^2$	0	1.18
	max growth $\sup_{t>0} \|\exp(-it\mathscr{L})\|$	$R/29.1$	$35.7/R$	1.60
Poiseuille	max resonance $\sup_{\omega\in\mathbb{R}} \|(\omega I - \mathscr{L})^{-1}\|$	$(R/17.4)^2$	0	1.62
	max growth $\sup_{t>0} \|\exp(-it\mathscr{L})\|$	$R/71.5$	0	2.04
Blasius	max resonance $\sup_{\omega\in\mathbb{R}} \|(\omega I - \mathscr{L})^{-1}\|$	$(R/1.83)^2$	0	0.21
	max growth $\sup_{t>0} \|\exp(-it\mathscr{L})\|$	$R/25.7$	0	0.65

TABLE 1. Maximum resonance and transient growth for selected shear flows and the corresponding streamwise α and spanwise β wavenumber. For Couette and Poiseuille flow the half channel width and the centreline velocity are used to make the quantities non-dimensional and for Blasius flow the displacement thickness and the free-stream velocity have that role. The values are taken from Trefethen *et al.* (1993), Butler & Farrell (1992) and P. J. Schmid (private communication).

instability, normally in the spanwise direction but for some cases in the wall-normal direction.

1.3. *Oblique transition*

Oblique transition is a transition scenario initiated by two oblique waves with opposite wave angle. We call these the $(1, \pm 1)$ modes, where the first 1 stands for the generated fundamental frequency in the spatial cases and for the fundamental streamwise wavenumber in the temporal cases. The second 1 stands for the fundamental spanwise wavenumber. Lu & Henningson (1990) first noted the growth potential of oblique disturbances in incompressible Poiseuille flow. Schmid & Henningson (1992) calculated oblique transition in channel flow using a temporal direct numerical simulation (DNS) code. They showed, for plane Poiseuille flow, that initial forcing and subsequent non-modal growth caused the rapid growth of the $(0, 2)$ mode. They calculated the relation between the energy transferred to the $(0, 2)$ mode by the nonlinear terms and the energy growth by non-modal linear mechanisms and found the latter to be the significant part. Joslin, Streett & Chang (1992, 1993) calculated oblique transition in an incompressible boundary layer using both parabolized stability equations (PSE) and spatial DNS. They chose two different amplitudes of the oblique waves. In the low-amplitude case the $(0, 2)$ mode grew rapidly and then decayed whereas they noted both the rapid growth of the $(0, 2)$ mode and a subsequent growth of other modes in the high-amplitude case. Berlin, Lundbladh & Henningson (1994) chose the parameters of the oblique waves to avoid any exponential instability in their spatial DNS calculation. They pointed out that the rapid non-modal growth of the $(0, 2)$ mode was associated with high- and low-speed streaks in the streamwise velocity component and conjectured that the onset of the growth of time-dependent modes was caused by secondary instability of the streaks when these reached a threshold value. For channel flow Reddy *et al.* (1998) found that the energy needed to initiate oblique transition is substantially lower than that needed in the transition scenarios caused by the two-dimensional TS-wave. Similar results have also been found in boundary layer flow by Schmid, Reddy & Henningson (1996).

Oblique transition has also been studied in compressible flows, where it is interesting to note that oblique modes are the linearly most unstable. Fasel & Thumm (1991) noted that oblique transition is a 'powerful process'. Using nonlinear PSE Chang &

Malik (1992, 1994) studied this scenario in a supersonic boundary layer and found oblique-wave breakdown to be a more viable route to transition and that it could be initiated by lower amplitude disturbances, compared to traditional secondary instability. Using DNS Fasel, Thumm & Bestek (1993) and Sandham, Adams & Kleiser (1994) studied oblique transition in compressible boundary layers and all investigators observed first the nonlinear interaction of the oblique waves generating the streamwise vortex mode (0, 2) and then its rapid growth. The fact that the rapid growth of the (0, 2) mode was caused by the non-normality of the linear operator discussed above was shown by Hanifi, Schmid & Henningson (1996) who also uncovered a compressible version of the inviscid algebraic instability (Hanifi & Henningson 1998).

The findings on transition mentioned above were all based on calculations. Experimentally, oblique transition has been investigated in Poiseuille flow by Elofsson & Alfredsson (1998) and by Wiegel (1996) and Elofsson (1998) in zero-pressure-gradient boundary layers. In the present investigation of oblique transition further details have been studied using both data from the experiments by Wiegel (1996) and numerical simulations. A similar comparison between experiment and simulation has been done for plane Poiseuille flow by Elofsson & Lundbladh (1994).

The tools used in the physical and numerical experiments are covered in § 2. Section 2.1 contains a description of the experimental set-up and the measurement techniques adopted for the present experiment and § 2.2 the numerical method. Results from experiments and simulations are compared in § 3 to explain the different stages of oblique transition. Oblique transition is compared to K- and H-type transition in § 4 and the reason for the similarities of the structures observed at the late transition stage are discussed. Concluding remarks are given in § 5.

2. Investigational tools

2.1. *Experimental method*

2.1.1. *Experimental set-up and measurement technique*

The experimental investigation was performed in the low-turbulence wind tunnel (TUG) at DLR Göttingen. It is an open wind tunnel with the fan at the inlet. A honeycomb and turbulence damping screens damp the turbulence level together with a plane 16 : 1 contraction to 0.065% for the wind speed of $U_\infty = 12\,\mathrm{m\,s^{-1}}$ that was used.

The measurements were performed on a flat Plexiglas plate 1500 mm wide, 1175 mm long and 40 mm thick, which was mounted vertically in the test section. The plate had an elliptic leading edge and a flap at the trailing edge. The device used to generate controlled three-dimensional disturbances is displayed in figure 1. It was situated 206 mm downstream of the leading edge and consisted of 40 slots, 10 mm wide and 0.3 mm in the streamwise direction, placed beneath each other with a spacing of 0.5 mm in the spanwise direction. Each slot led to a pressure chamber inside the plate, in which pressure fluctuations from a loudspeaker were introduced through a plastic tube. We make use of the effect that small periodic pressure oscillations produced by the loudspeakers cause small periodic velocity fluctuations which can be used for a well-defined excitation of the boundary layer. A signal generator with 20 channels followed by amplifiers supplied the excitation signals for the loudspeakers. It was possible to address each loudspeaker separately; however, all channels were phase-locked. By prescribing the phase shift between the channels one or two oblique

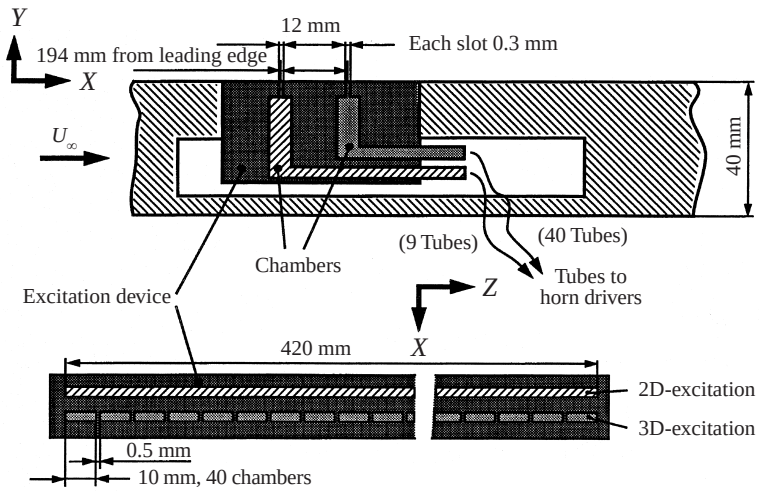

FIGURE 1. Device for disturbance generation. Note that the distance to the virtual leading edge is 20 mm less than the distance to the actual leading edge given in the figure.

waves could be generated. More details of the set-up and the excitation device can be found in Wiegel (1996).

Detailed measurements were then made by both hot-wire anemometry and particle image velocimetry (PIV). Flow visualizations gave a good overview of the transition scenario and were useful for choosing suitable spanwise wavelength, frequency and amplitude for the oblique waves. For PIV measurements and flow visualizations a laser system created a light sheet, which was aligned parallel to the surface of the plate and could be manually scanned through the boundary layer. The light sheet was 0.6 mm thick and illuminated tracer particles in the observation area stroboscopically with a repetition rate of 10 Hz. Each illumination actually consisted of two light pulses with a duration of 20 ns. The time delay between the two pulses could be varied in a wide range but for our set-up it was chosen as 100 μs. The mean diameter of the tracer particles in the flow was approximately 1 μm and the seeding rake was located upstream of the turbulence damping screens. The pictures could be recorded with a CCD camera or with a standard 35 mm camera. The recorded area was of the order of 0.2 m by 0.1 m. The signal of the CCD camera was digitized by means of a frame grabber. The frame grabber, or the shutter release of the 35 mm camera, and the laser light pulse, were triggered by the signal generator for the excitation, so that a fixed phase relation between excitation and recorded picture was guaranteed. It was also possible to set an additional phase shift to acquire pictures at various phases over one period. The uncertainty of the velocity readings produced by the evaluation procedure used is well below 1% of the mean flow velocity.

A three-axis traversing system was used for single hot-wire sensors. The traversing mechanisms were driven by computer-controlled stepper motors with a wall-normal resolution of 0.001 mm and a spanwise resolution of 0.01 mm. Velocity, temperature, and dynamic pressure data were directly digitized through a 12-bit A/D converter. The fluctuating velocities at the desired frequency were filtered in a 1 Hz bandpass by computing the autospectral density function using an FFT. The cross-spectrum between the hot-wire signal and the forcing signal of the signal generator provided phase information.

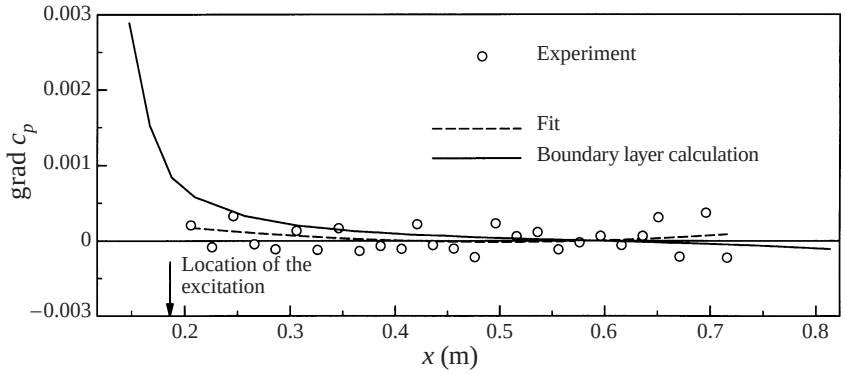

FIGURE 2. Pressure gradient in streamwise direction without excitation, $z = 0$.

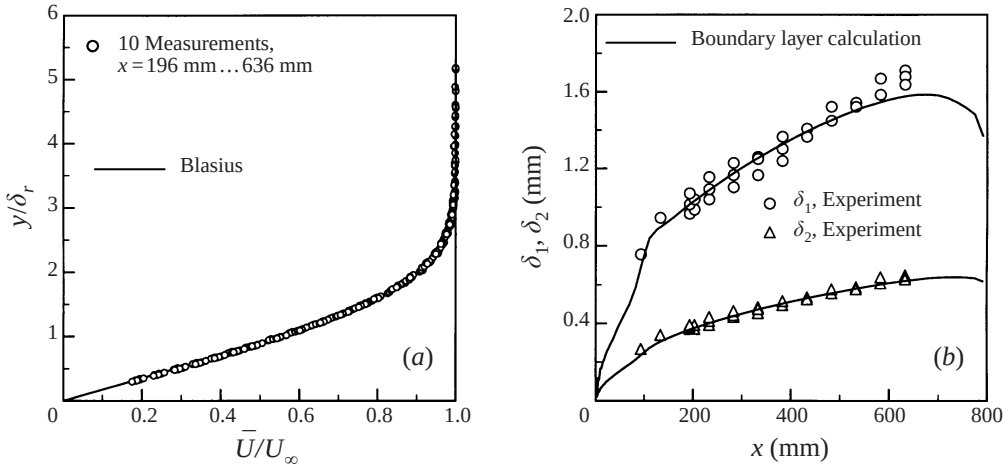

FIGURE 3. (*a*) Mean velocity profile, (*b*) variation of the integral flow parameters, δ_1 and δ_2, without excitation.

2.1.2. *Flow quality and wave parameters*

The flap at the trailing edge of the plate was adjusted to achieve as close to a zero-pressure-gradient boundary layer in the measurement region as possible. The measured pressure gradient is presented in figure 2 and the scatter of order 0.001 in the experimental data around the fit is probably due to low-frequency velocity fluctuations. For comparison the predicted pressure gradient from a boundary layer calculation is presented. The boundary layer program (Rotta 1971) accounts for the shape of the leading edge but not the walls of the wind tunnel and the flap. It takes the pressure distribution from a potential flow solution as in data. As the boundary layer develops under a pressure gradient around the leading edge the boundary layer thickness at a certain downstream coordinate will differ from that of a theoretical Blasius boundary layer. Therefore a virtual leading edge is calculated from the actual displacement thickness in the measurement region to fit a theoretical leading edge. This is situated 20 mm downstream of the real leading edge and we will from now on refer all downstream distances to the virtual leading edge both in the experimental and numerical results presented. All wall-normal coordinates y will either be normalized by the Blasius reference length $\delta_r = (\nu x/U_\infty^2)^{1/2}$ at the local x or be given in millimetres.

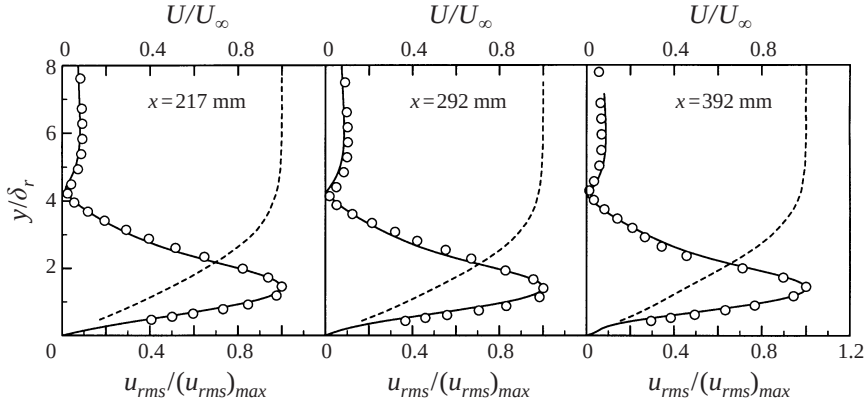

FIGURE 4. Mode shape at various downstream locations for $f = 90$ Hz and $U_\infty = 12\,\mathrm{m\,s^{-1}}$, solid lines represents linear theory and dashed lines mean velocity.

Figure 3 displays the velocity profiles achieved in the measurement section as well as the downstream development of the displacement thickness. This figure also shows that we can assume a Blasius boundary layer downstream of the excitation. The spanwise spectra of the undisturbed mean flow of both the free stream and boundary layer were checked to make sure that there were no peaks at the spanwise wavelengths excited later in the experiment.

The excitation device introduces locally a wall-normal velocity but the goal is to have controlled oblique eigenmodes moving downstream. Therefore the calibration of the excitation is based on measuring the disturbance level inside the boundary layer downstream of the excitation. Setting the same phase of the excitation signal for all 40 slots a two-dimensional wave was generated, which made it possible to check that the amplitude was evenly distributed in the spanwise direction. The frequency of the generated oblique waves was 90 Hz corresponding to a non-dimensional frequency in the current setting of $F = 59$ ($F = 2\pi f\nu/(U_\infty^2 \times 10^{-6})$) and setting the phase shift between adjacent slots to $\pm 60^\circ$ a spanwise wavelength of 63 mm was obtained. The mode shape of the generated waves was compared to that calculated by linear theory and good agreement was found as shown in figure 4, where also the mean velocity profiles are displayed.

Setting frequency and spanwise wavelength the wave angle was found from flow visualizations to be $35 \pm 3^\circ$, well in accordance with the theoretical value of 38°. The fact that the generation device was directly forcing the desired eigenmode was established by showing that the amplitude of the oblique waves was a linear response of the excitation amplitude A. This is shown in figure 5(b), where A is linearly related to the loudspeaker input. A bandpass filter selected the frequency of the oblique waves for the u_{rms} displayed in the figure and as the measurements were made close ($x = 217$ mm) to the disturbance generation device higher harmonics had very low amplitude. Figure 5(a) demonstrates that the mode shape was independent of the forcing amplitude.

2.2. *Numerical method*

2.2.1. *Numerical scheme*

The simulation code (see Lundbladh, Henningson & Johansson 1992 and Lundbladh *et al.* 1994) used for the present computations uses spectral methods to solve

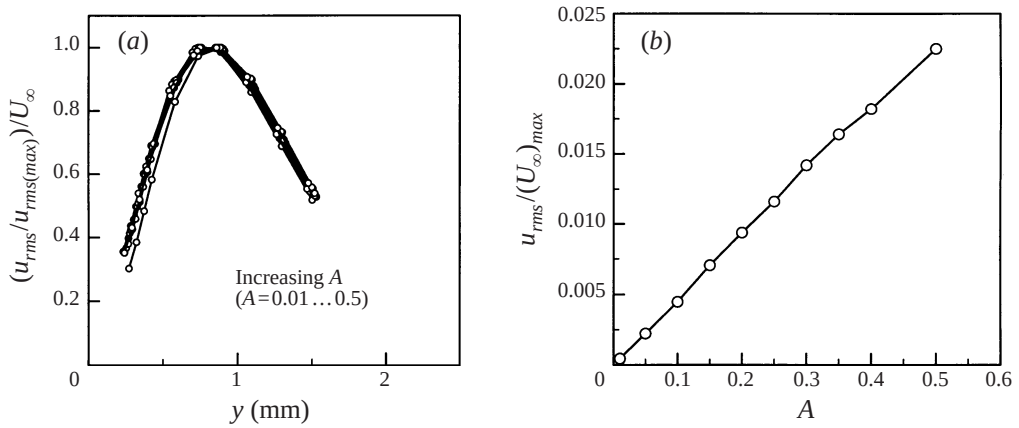

FIGURE 5. (*a*) Wall-normal variation of the normalized u_{rms} for various excitation levels. (*b*) Maximum of u_{rms} at $x = 217$ mm and $z = 0$ mm amplitude versus excitation level.

the three-dimensional, time-dependent, incompressible Navier–Stokes equations. The algorithm is similar to that of Kim, Moin & Moser (1987), i.e. Fourier representation in the streamwise (x) and spanwise (z) directions and Chebyshev polynomials in the wall-normal (y) direction and pseudo-spectral treatment of the nonlinear terms. The time advancement used was a four-step low-storage third-order Runge–Kutta method for the nonlinear terms and a second-order Crank–Nicholson method for the linear terms. Aliasing errors from the evaluation of the nonlinear terms were removed by the $\frac{3}{2}$-rule when the FFTs were calculated in the wall-parallel plane. In the wall-normal direction we have found it more efficient to increase resolution rather than using dealiasing.

To correctly account for the downstream boundary layer growth and pressure gradient effects a spatial technique is necessary. That requirement was combined with the periodic boundary condition in the streamwise direction by the implementation of a 'fringe region', similar to that described by Bertolotti, Herbert & Spalart (1992). In this region, at the downstream end of the computational box, the function $\lambda(x)$ is smoothly raised from zero and the flow is forced to a desired solution $\boldsymbol{v}$ in the following manner:

$$\frac{\partial \boldsymbol{u}}{\partial t} = NS(\boldsymbol{u}) + \lambda(x)(\boldsymbol{v} - \boldsymbol{u}) + \boldsymbol{g}, \tag{2.1}$$

$$\nabla \cdot \boldsymbol{u} = 0, \tag{2.2}$$

where $\boldsymbol{u}$ is the solution vector and $NS(\boldsymbol{u})$ the right-hand side of the (unforced) momentum equations. Both $\boldsymbol{g}$, which is a disturbance forcing, and $\boldsymbol{v}$ may depend on the three spatial coordinates and time; $\boldsymbol{v}$ is smoothly changed from the laminar boundary layer profile at the beginning of the fringe region to the prescribed inflow velocity vector. This is normally a boundary layer profile of a chosen Falkner–Skan flow, but can also contain a disturbance. A convenient form of the fringe function is

$$\lambda(x) = \lambda_{max}\left[S\left(\frac{x - x_{start}}{\Delta_{rise}}\right) - S\left(\frac{x - x_{end}}{\Delta_{fall}} + 1\right)\right]. \tag{2.3}$$

Here λ_{max} is the maximum strength of the damping, x_{start} to x_{end} the spatial extent of the region where the damping function is non-zero and Δ_{rise} and Δ_{fall} the rise and

fall distance of the damping function. $S(x)$ is a smooth step function rising from zero for negative x to one for $x \geqslant 1$. We have used the following form for S, which has the advantage of having continuous derivatives of all orders:

$$S(x) = \begin{cases} 0, & x \leqslant 0 \\ 1/\left[1 + \exp\left(\dfrac{1}{x-1} + \dfrac{1}{x}\right)\right], & 0 < x < 1 \\ 1, & x \geqslant 1. \end{cases} \tag{2.4}$$

This method damps disturbances flowing out of the physical region and smoothly transforms the flow to the desired inflow state, with a minimal upstream influence.

In order to set the free-stream boundary condition closer to the wall, a generalization of the boundary condition used by Malik, Zang & Hussaini (1985) was implemented. Since it is applied in Fourier space with different coefficients for each wavenumber, it is non-local in physical space and takes the form

$$\frac{\partial \hat{\boldsymbol{u}}}{\partial y} + |k|\hat{\boldsymbol{u}} = \frac{\partial \hat{\boldsymbol{v}}_0}{\partial y} + |k|\hat{\boldsymbol{v}}_0. \tag{2.5}$$

Here k is the absolute value of the horizontal wavenumber vector and $\hat{\boldsymbol{u}}$ is the Fourier transform of $\boldsymbol{u}$. The Fourier transform $\hat{\boldsymbol{v}}_0$ of $\boldsymbol{v}_0$ is usually the local solution to a Falkner–Skan flow, with the streamwise free-stream velocity varying as

$$U = U_0 x^m. \tag{2.6}$$

$\boldsymbol{v}_0$ can also be chosen arbitrarily in order to simulate other pressure variations than those found in Falkner–Skan flow. On the wall the boundary condition is either no slip or a time-dependent wall-normal velocity.

2.2.2. *Disturbance generation and box dimensions*

The presented numerical implementation provides several possibilities for disturbance generation. Oblique waves with an angular frequency $\omega_0 = 2\pi$ 90 Hz and a spanwise wavenumber of $\beta_0 = 99.73$ m^{-1} has in this investigation been generated with five different methods. In the presentation of results we will transform the non-dimensional variables used in the simulation code to dimensional ones, using the kinematic viscosity for air and free-stream velocity $U_\infty = 12$ m s^{-1}. We will also refer the downstream coordinate x to the virtual leading edge of the experiment. We have given the five different generation methods of oblique waves the following abbreviations:

FRIN Generation in the fringe region by adding the least-damped Orr–Sommerfeld mode for the chosen parameters to the forcing vector $\boldsymbol{v}$ in equation (2.1). The computational box was in this case designed such that the inflow was at $x = 186$ mm.

BODY Generation by a body force. In the volume $184 \leqslant x \leqslant 187$ mm, $0 \leqslant y \leqslant 1.55$ mm $\boldsymbol{g}$ was assigned to: $g_x = A\cos(\beta_0 z)\cos(\omega_0 t)/(2\omega_0)$, $g_y = A\cos(\beta_0 z)\sin(\omega_0 t)$, $g_z = -A\sin(\beta_0 z)\sin(\omega_0 t)/(2\beta_0)$, where the amplitude A was smoothly reduced to be zero at the top boundary of the forcing volume.

BLOW Generation by blowing and suction. The wall-normal velocity component (v) in the interval $184 \leqslant x \leqslant 187$ mm was on the wall specified as $v = A\cos(\beta_0 z)\sin(\omega_0 t)$.

STEP Generation by stepwise blowing and suction. The wall-normal velocity component in the interval $184 \leqslant x \leqslant 187$ mm was on the wall set to vary as $v = A\,\mathrm{step}(z)\sin(\omega_0 t)$, where the 'step' function for each spanwise wavelength has six levels: 1, 0.5, −0.5, −1, −0.5, 0.5. The change-over between the levels was smooth.

	$x1 \times y1 \times z1$ (mm)	$nx \times ny \times nz$ (resolution)	Forcing u_{rms}%
Box 1	$775 \times 11.6 \times 63$	$1200 \times 65 \times 96$	1.4
Box 2	$397 \times 11.6 \times 63$	$512 \times 65 \times 80$	2.3
Box 3	$310 \times 11.6 \times 63$	$512 \times 65 \times 120$	2.3
Box 4	$310 \times 11.6 \times 63$	$720 \times 97 \times 192$	2.3

TABLE 2. Resolution and box dimensions for the simulations presented. The box dimensions include the fringe region, which took up 62 mm at the downstream end of the box in all cases. $z1$ and nz representes the full span and the total number of Fourier modes, respectively. In the actual computations these numbers could be halved since the flow is symmetric. The forcing is given as the u_{rms} of the oblique waves at $x = 217$ mm.

DAMP Generation by blowing and damped suction. The wall-normal velocity component in the interval $184 \leqslant x \leqslant 187$ mm was on the wall set to vary as

$$v = \max(A \cos(\beta_0 z) \sin(\omega_0 t), A\, d \cos(\beta_0 z) \sin(\omega_0 t)), \tag{2.7}$$

where $0 \leqslant d \leqslant 1$ is a damping factor reducing negative values of the wall-normal velocity at the wall.

The DNS code for the boundary layer geometry is a development of the channel code by Lundbladh *et al.* (1992), which has been extensively tested and used. To verify the spatial boundary layer version comparisons have been made with the results reported by Fasel & Konzelmann (1990). It was also possible to compare with linear parallel theory by adding a body force:

$$\boldsymbol{g} = -\frac{1}{R}\frac{\partial^2 U(x,y)}{\partial y^2}, \tag{2.8}$$

which produces a parallel mean flow in the whole computational domain.

The box sizes and resolutions used for the simulations presented in this paper are displayed in table 2. The displacement thickness at the position where the oblique waves were generated was 0.83 mm and this was 30 mm downstream of the inflow boundary in all but the FRIN case. The width of the box was set to fit one spanwise wavelength of the oblique waves. Since an initial symmetry is preserved by the Navier–Stokes equations we could save computational costs by only calculating one half of each wall-parallel (x, z) plane. Box 1 was used for the calculations presented in § 3.1.1 and § 3.1.2. The lower forcing amplitude was used to prolong the transition development and clarify the initial part. The flow visualization presented in § 3.1.1 was also made with a lower forcing amplitude. The transition stages and development observed were the same as for the other cases. Box 2 was used for the simulations in § 3.1.3 and § 3.2. The flow in Box 1 and Box 2 did not reach as far in the transition process as in the other two cases and the calculations were therefore over-resolved. Box 3 and Box 4 were used for the results in § 3.3 and § 3.4. The amplitudes of the disturbances and the flow observed in these cases were the same, but the resolution of Box 3 was marginal whereas that of Box 4 was sufficient, which we concluded after finding the most energetic structures in the end of the box at identical positions and with a difference in the streamwise shear of less than 1%.

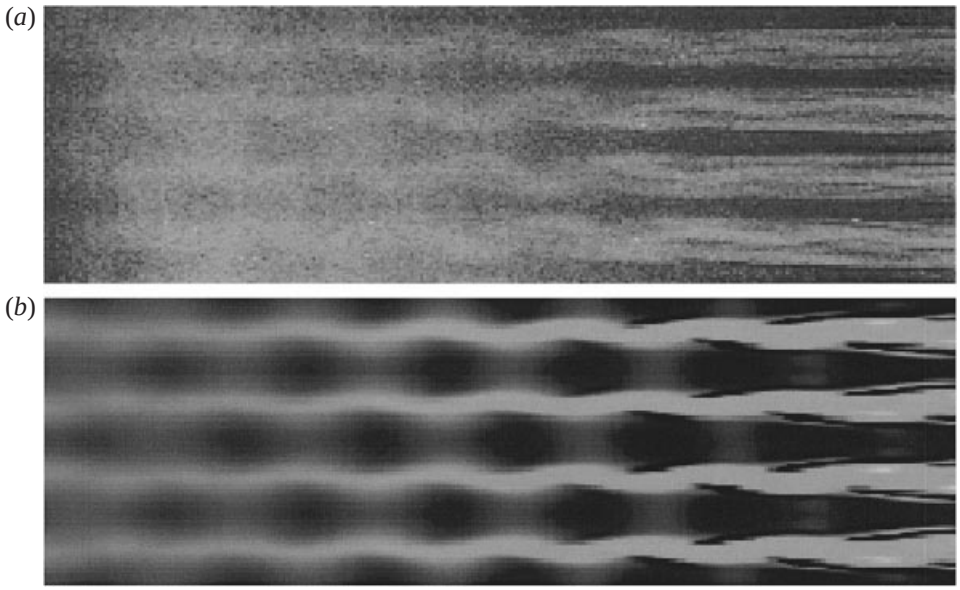

FIGURE 6. (*a*) Photo from flow visualization of oblique transition. (*b*) Instantaneous streamwise velocity from numerical simulation, plane parallel to the wall, flow from left to right.

3. Results

In order to better demonstrate the coherence of experiment and simulations, we sometimes present data from both investigations in the same figure. In general, we want to give a good description of oblique transition and therefore alternate experimental and DNS results depending on what is most suitable for describing a certain property. The presentation of results in § 3.1 shows the basic mechanisms of oblique transition and establishes that we observe the same qualitative development in both experiment and calculations. In § 3.2 we present a numerical investigation of how the different disturbance generation techniques and changes in the pressure gradient affect the transition scenario. Those results are in § 3.3 used to closely model the experiment using the DNS. Finally a combination of numerical and DNS results is used in § 3.4 to give a good picture of the late stage of oblique transition.

3.1. *Basic features*

3.1.1. *The emergence of large-amplitude streaks*

The photograph from a flow visualization in figure 6(*a*) displays the dominating feature of oblique transition: spanwise-periodic streamwise streaks growing inside the boundary layer. These are associated with regions of low- and high-speed streamwise velocity and a snapshot of this velocity component from a simulation displays a similar picture (figure 6*b*). The comparison is qualitative and the amplitude of the initiated oblique waves may be different in the two figures. The results presented in this subsection mostly originate from experiments and simulations with weak forcing of the oblique waves. This prolongs the initial development in the streamwise direction and the initially generated oblique waves are therefore clearly noticed as a checkboard pattern of dark and light patches in the left upstream part in figure 6(*a,b*). The development of the oblique waves is, however, easier to study when the

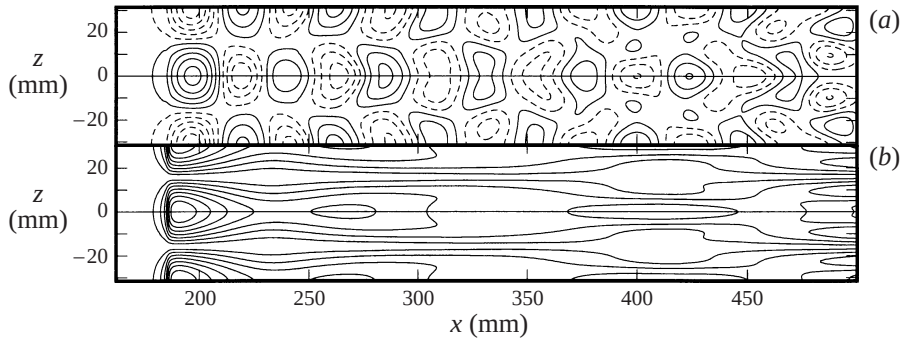

FIGURE 7. (*a*) Fluctuating streamwise velocity $\tilde{\boldsymbol{u}}$ at $y = 0.98$ mm, contour spacing 0.005. (*b*) Contours of u_{rms} at $y = 0.98$ mm, spacing 0.0025.

time-averaged mean streamwise velocity U is subtracted from the flow field, thus removing the steady streaks from the velocity.

In figure 7(*a*), where only the fluctuating part of the streamwise velocity $\tilde{u} = \tilde{u}(t, x, y, z)$ remains, the oblique waves are seen to decay slowly after the generation point. Further downstream the pattern changes as disturbances with higher spanwise wavenumber reach an amplitude comparable to that of the oblique waves. Since the alternating maxima and minima of the oblique waves are aligned in the streamwise direction, the root mean square of the streamwise velocity (u_{rms}) will also show structures aligned in the streamwise direction (figure 7*b*).

The nonlinear interaction of the oblique waves generates counter-rotating streamwise vortices. The time-averaged mean of the streamwise vorticity is shown in figure 8(*a,d*) together with the mean of the wall-normal and spanwise velocity components (figure 8 *b,c*). The spanwise wavelength of the vortex pattern is half that of the oblique waves. The vortices decay downstream, but in spite of that they generate the growing high- and low-speed streaks by the *lift-up* mechanism described in the introduction. By subtracting the spanwise mean from the mean streamwise velocity in both experiment and simulation and plotting in a plane perpendicular to the flow, comparable figures of the streamwise velocity perturbation are shown in figure 9(*a,b*). The small arrows symbolize the rotation direction of the associated vortices.

If the amplitude of the initiating oblique waves is to low, the streak amplitude will grow and thereafter decay, but for larger amplitudes transition to turbulence will be observed. The forcing amplitude was low in previous figures to prolong the initial development of the oblique waves and the streaks and transition occurred downstream of the measurement domain. For the results presented in figure 10 and in all other Sections, the initial amplitude of the oblique waves was increased to move the fully turbulent region upstream. Figure 10 shows wall-normal profiles of streak amplitude for several downstream positions in the experimental set-up. The shape is the same as the so-called Klebanoff mode (Klebanoff 1971; Kendall 1985), which consists of low-frequency oscillations observed in boundary layers subjected to free-stream turbulence. The maxima of the profiles are found at a constant y/δ_r. The streak amplitude decreases after $x = 467$ mm when the disturbance level in the flow reaches high values (figure 10*b*) and the maximum of the wall-normal profile moves away from the wall (figure 10*a*).

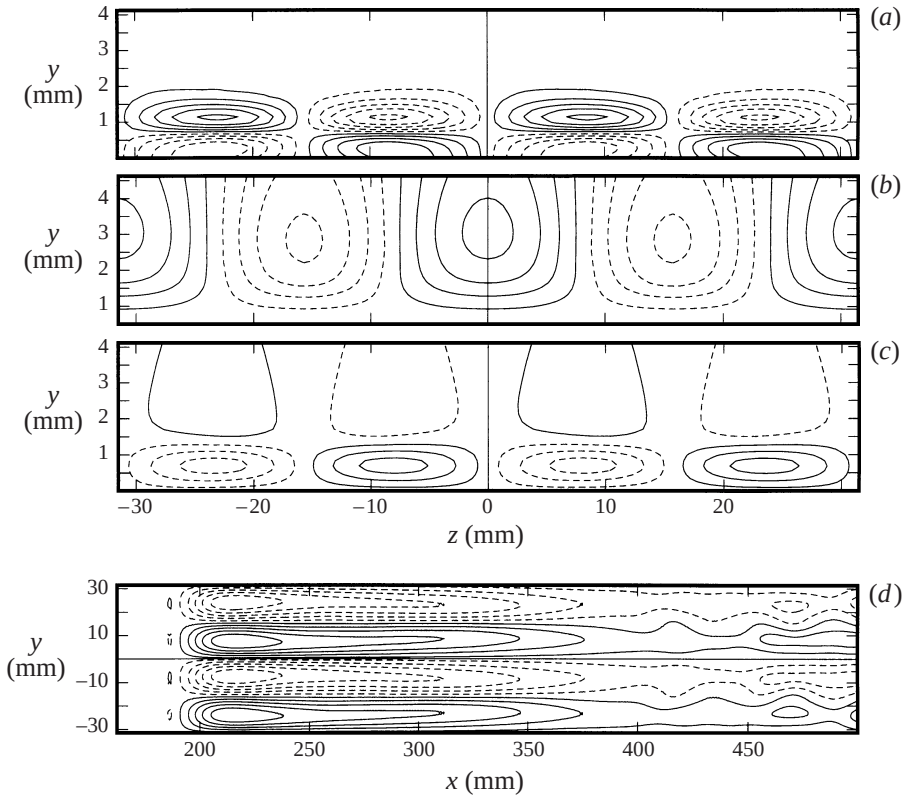

FIGURE 8. Mean quantities from which a laminar Blasius flow has been subtracted. (*a*) Contours of streamwise vorticity $\bar{\omega}_x$ with 2×10^{-4} steps. (*b*) Contours of wall-normal velocity $\bar{v}$ with 0.5×10^{-4} steps. (*c*) Contours of spanwise velocity $\bar{w}$ with 2×10^{-4} steps. (*d*) Contours of streamwise vorticity $\bar{\omega}_x$ with 2.5×10^{-4} steps. (*a–c*) In the plane $x = 317$ perpendicular to the flow and (*d*) in wall-parallel plane $y = 0.98$ mm.

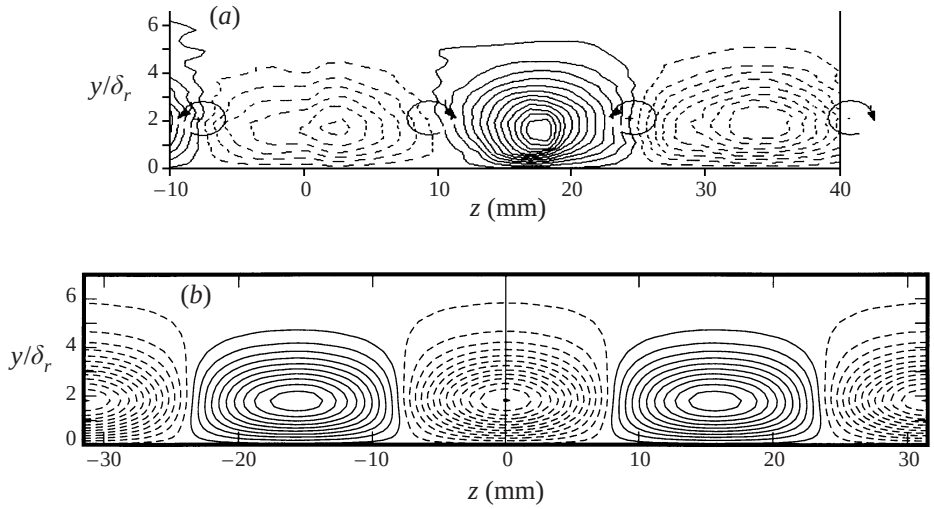

FIGURE 9. Contours of mean streamwise velocity disturbance: (*a*) experiment (*b*) simulation; solid lines represent positive values and dashed negative values.

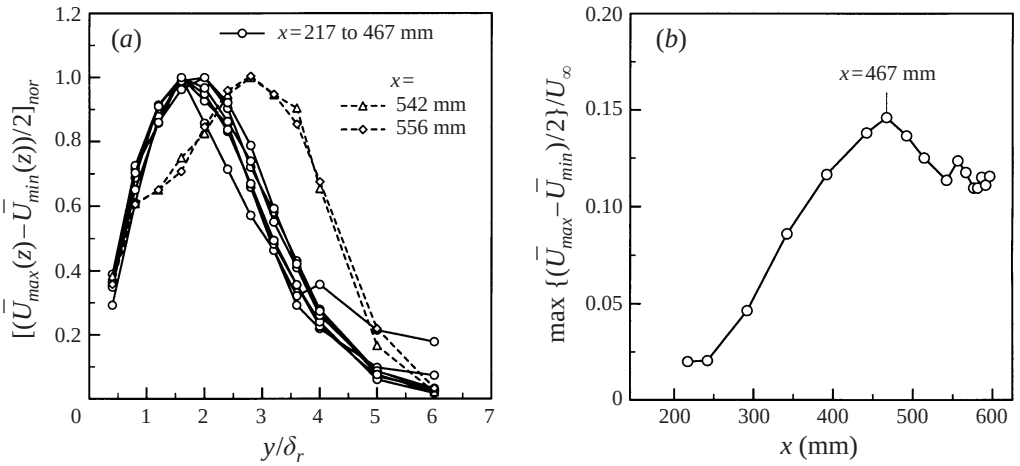

FIGURE 10. (*a*) Variation of the streak amplitude in the wall-normal direction at several downstream positions. (*b*) Development of the streak amplitude in the streamwise direction.

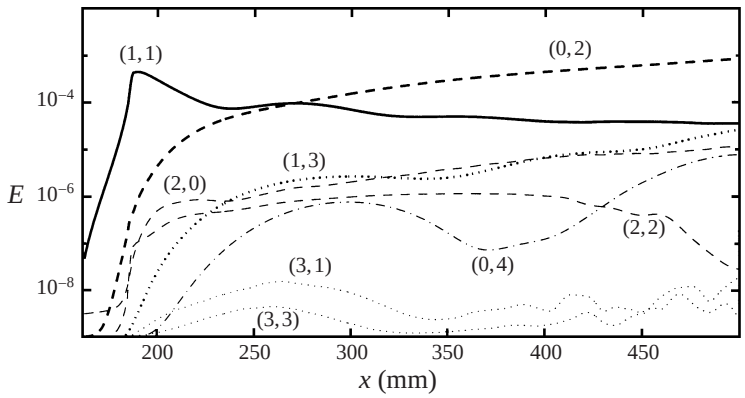

FIGURE 11. Energy in the initially generated Fourier mode (1, 1) (solid line). The modes exited after the first generation of nonlinear interaction (0, 2), (2, 2) and (2, 0) (dashed lines). Modes exited after the second step of nonlinear interactions are dotted lines, (1, 3), (3, 3) and (3, 1). Dash dotted lines are (0, 4).

3.1.2. *Development of Fourier components*

We transform the velocity fields in time and in the spanwise direction to Fourier space and use the notation (ω, β), where ω and β are the frequency and spanwise wavenumber respectively, each normalized with the corresponding fundamental frequency/wavenumber. Thus the oblique waves are represented by $(1, 1)$ and $(1, -1)$ and the streaks by $(0, 2)$. In figure 11 the slow decay of $(1, 1)$ after the peak at the generation point $x = 186$ mm is clear as well as the upstream influence of the generation. As the flow is symmetric and (ω, β) equal to $(\omega, -\beta)$, we only show modes with positive β. The first generation of nonlinearly excited modes $(2, 0)$, $(2, 2)$ and $(0, 2)$ are represented by dashed lines and the the second generation modes $(3, 1)$, $(3, 3)$ and $(1, 3)$ are dotted. According to the results on non-modal growth, disturbances with zero or low frequency should have the greatest growth potential, which is precisely what we find. The $(0, 2)$ and $(1, 3)$ modes gain approximately two orders of magnitude more energy than the other modes of their respective nonlinear generation. This is

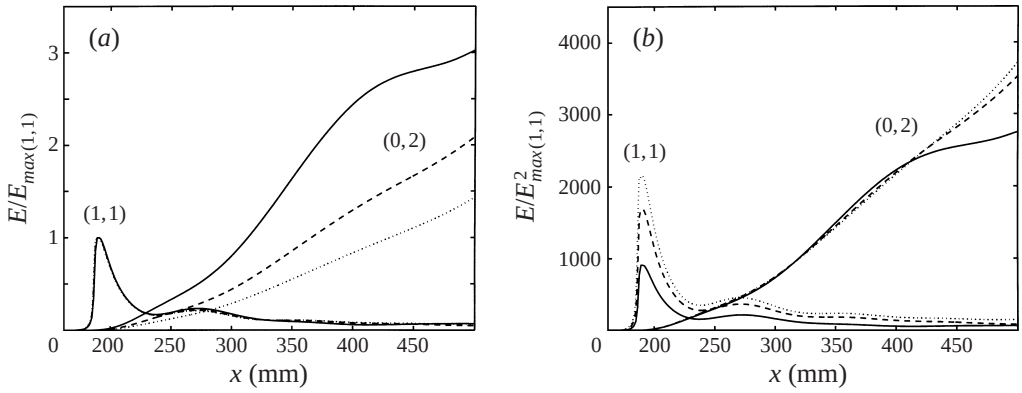

FIGURE 12. Energy in $(1,1)$ and $(0,2)$ components from simulations with increasing initial waveamplitude, dotted curves correspond to the lowest amplitude and solid to the highest: (*a*) curves scaled with $\max(1,1)$, (*b*) curves scaled with $\max(1,1)^2$.

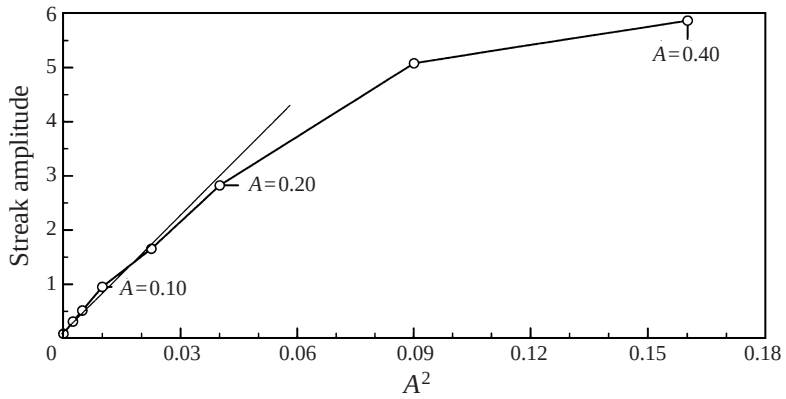

FIGURE 13. Streak amplitude at $x = 478$ mm in the experiment as function of the squared forcing amplitude of oblique waves, showing the quadratic dependence of the streak response on the forcing. At higher forcing amplitudes the streaks saturate and therefore do not follow the quadratic behaviour.

also true for the $(0,4)$ mode which is the only mode of higher nonlinear generation displayed in figure 11. After $x = 350$ mm the curves representing the $(1,1)$ and $(1,3)$ modes approach each other, which is also evident in figure 7(*a*) where the fluctuating velocity field is gradually complicated by shorter spanwise wavelengths.

3.1.3. *Quadratic dependence of streak amplitude*

In figure 12 the development of the energy in the $(1,1)$ and $(0,2)$ modes is compared using simulations with three different initial wave amplitudes. If the amplitudes are scaled with the maximum of $(1,1)$ for each run (figure 12*a*), the $(1,1)$ curves collapse showing the linear relation between the forcing and the downstream amplitude. The energy in $(0,2)$ for the case with the strongest initial forcing reaches a level where nonlinear saturation occurs at approximately $x = 400$ mm. Scaling with the maximum of $(1,1)$ squared instead, as in 12(*b*), the $(0,2)$ curves collapse up to the downstream position of saturation, showing the quadratic nonlinear generation of $(0,2)$ from $(1,\pm1)$.

The same observations can be made in the experiment. It was shown in figure 5(*b*)

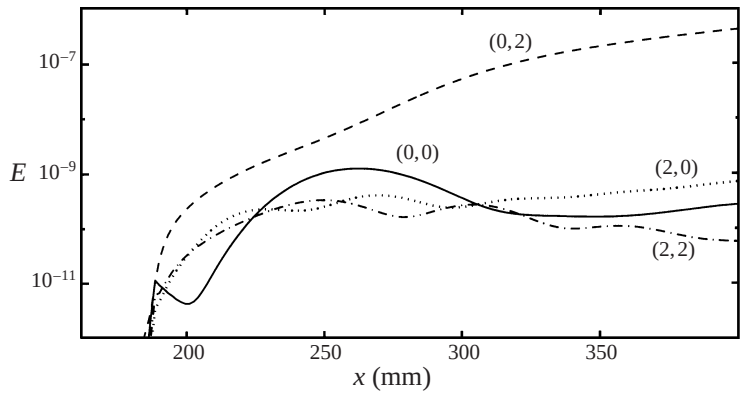

FIGURE 14. Energy relation between the quadratic part of the first nonlinearly generated modes. Note the additional growth in (0, 2) caused by the non-modal effects.

that the oblique waves scale linearly with the forcing amplitude of the loudspeakers. The streak amplitude depends quadratically on the forcing amplitude in the experimental investigation, see figure 13, where the streak amplitude at a fixed downstream position is plotted against the square of the forcing amplitude. The experimental curve follows the straight line until the forcing is strong enough to cause nonlinear saturation of the streaks.

3.1.4. *Non-modal effects*

The initial behaviour of the nonlinearly generated Fourier modes shows the presence of non-modal effects in the amplification and growth. To make this point clear we show in figure 14 the quadratic part of the first generation nonlinearly generated modes, i.e. (0, 2), (2, 2), (2, 0) and (0, 0), extracted using the numerical amplitude expansion technique developed in Henningson, Lundbladh & Johansson (1993). First note that all four modes appear to be generated simultaneously by the nonlinear interaction of the two oblique waves. Second, it is apparent that the response to the nonlinear forcing by the oblique waves is very different. The (2, 0) and the (2, 2) components, which are damped and not associated with large non-normal effects, stay at a rather low level during the simulation. The (0, 0) component which is less damped, but for which all wall-normal eigenfunctions are orthogonal, experience a slightly larger growth after the initial generation. However, the (0, 2) component, that has a damping similar to the (0, 0) component, dominates since it can be forced to high amplitude by moderate forcing. This non-modal effect is associated with the highly non-orthogonal set of eigenfunctions present for this Fourier component. These results are consistent with the bounds on the response to forcing presented in § 1.2, although here we are dealing with spatial rather than temporal growth.

3.2. *Dependence of the disturbance evolution on physical and numerical parameters*

In this section we will discuss how the flow reacts to changes of input parameters and how to understand discrepancies between experiment and simulation.

3.2.1. *Effects of different disturbance generation methods*

R.m.s. dependence

Both an experimental and a numerical investigator may consider different designs or methods for disturbance generation. We have therefore compared the five gen-

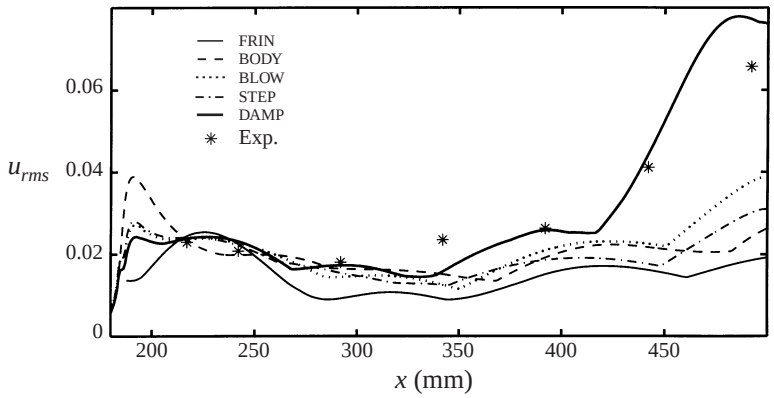

FIGURE 15. Downstream development of u_{rms} for the five different generation methods of the oblique waves and experimental results.

eration methods mentioned in § 2.2 and the experimental results. An experimental correspondence to the FRIN method is hard to think of, but BLOW, STEP and DAMP are certainly connected to experimental blowing and suction devices and the BODY method could be connected to an experiment with vibrating ribbons. Indeed Elofsson & Lundbladh (1994) managed to closely model vibrating ribbons in a channel flow by the use of an oscillating body force.

Figure 15 shows the downstream development of the r.m.s. amplitude in the streamwise velocity component (u_{rms}) for the five different generation methods as well as for the experiment. The strength of the generation in the simulations was set such that the maximum u_{rms} at $x = 217$ mm was equal to the experimentally measured value at that position. The signal in both the experiment and the simulation was filtered to select the generation frequency, and in the following the curves of u_{rms} will only contain that frequency. The difference between the total u_{rms} and the filtered u_{rms} in the simulations presented in this section never exceeded 14% and that occurs when the flow is almost turbulent.

The overall downstream development of u_{rms} is similar for all five cases, despite the fact that the initial development strongly depends on the type of forcing and that matching was done at a single downstream position. The curve for the FRIN case lies slightly below the others and u_{rms} grows significantly more after $x = 400$ mm in the DAMP case. The damping factor of suction in the DAMP simulation presented in this section was $d = 0.4$.

R.m.s. modes and their phase

In frequency–wavenumber space the modes contributing to the filtered u_{rms} will be $(1, \beta)$, where β is any integer. Note that as the flow is symmetric the modes (ω, β) and $(\omega, -\beta)$ have the same amplitude and in the following we will denote the sum of these modes by $(1, \pm\beta)$. We find that the dominating modes are $(1, \pm 1)$, $(1, \pm 3)$ and $(1, \pm 5)$. Figure 16 shows u_{rms} and the r.m.s. of these modes of the BLOW case together with the phase difference between the $(1, 1)$ and the $(1, 3)$ modes. The generated $(1, \pm 1)$ mode decays downstream but the $(1, \pm 3)$ and $(1, \pm 5)$ modes grow and after $x = 380$ mm $(1, \pm 3)$ dominate. The phase relation explains the local extrema appearing in the u_{rms} curve, where a minimum appears when the phase shift is $\pm\frac{1}{2}\pi$ and a maximum when it is 0. The extremum

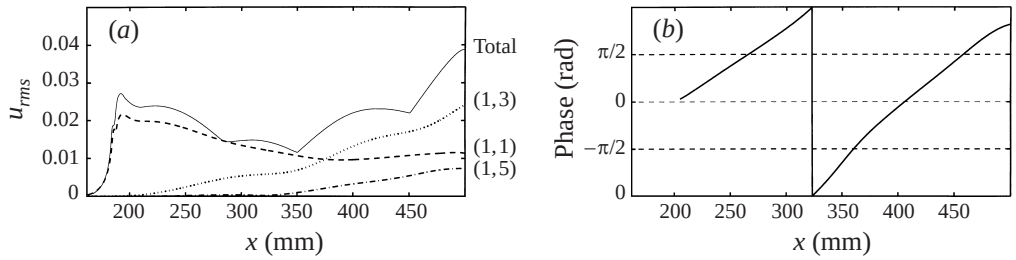

FIGURE 16. (*a*) Filtered u_{rms} and r.m.s. of the $(1,1)$, $(1,3)$ and $(1,5)$ modes for a case with oblique waves generated by blowing and suction, BLOW. (*b*) Phase difference between the $(1,1)$ and $(1,3)$ modes. Note the correspondence between zero and $\pm\pi/2$ phase shift and the local extrema in the u_{rms} curve.

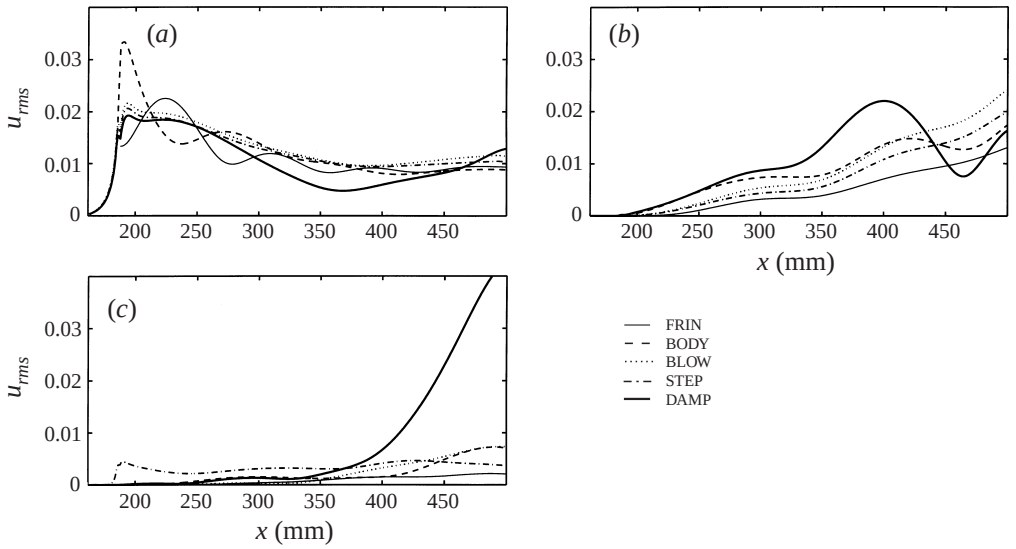

FIGURE 17. u_{rms} for various modes: (*a*) $(1,\pm1)$ mode, (*b*) $(1,\pm3)$ mode, (*c*) $(1,\pm5)$ mode, and the different generation methods.

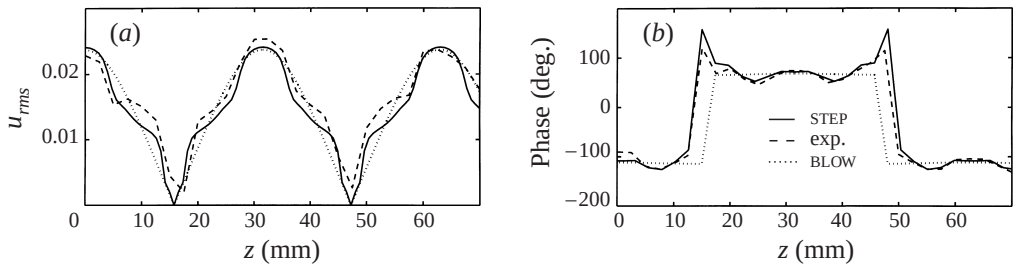

FIGURE 18. Spanwise variation of (*a*) u_{rms} and (*b*) phase from STEP (—), experiment (- -) and BLOW ($\cdots$).

is sometimes slightly off the location with $\pm\frac{1}{2}\pi$ or 0 phase shift, which is caused by the fact that $(1,1)$ mode is decaying and the $(1,3)$ one increasing.

To further study the differences between the generation methods, the dominating frequency–wavenumber modes are compared in figure 17. It is clear that the down-

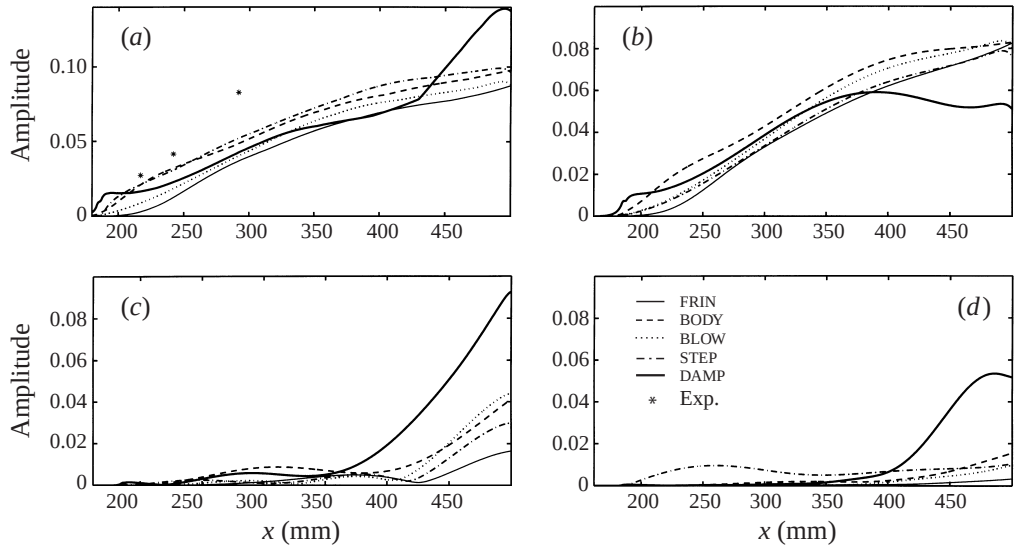

FIGURE 19. (*a*) Streak amplitude, (*b*) (0, 2) mode, (*c*) (0, 4) mode and (*d*) (0, 6) mode for different generation methods and experiment.

stream differences in the filtered u_{rms} are accounted for by the higher modes $(1, \pm 3)$ and $(1, \pm 5)$. Particularly, the strong growth in the DAMP case is associated with the $(1, \pm 5)$ modes. Significant initial generation of the $(1, \pm 5)$ modes in the STEP case is observed in figure 17(*c*). Comparing with the experimental results one finds that generation with a stepwise amplitude variation in the spanwise direction is necessary to get close agreement. This is illustrated in figure 18 where the spanwise variation of both u_{rms} and the phase are plotted. The u_{rms} curve for both the experiment and the STEP simulation show a typical bottle shape, caused by the (1, 5) mode. Results from a simulation with a sinusoidal spanwise blowing and suction have been included in the figure as reference and this has a square-wave-like phase curve, to compare with the curves including sharp peaks corresponding to the stepwise results.

Streak dependence

The differences in generation of the oblique waves and the growth of the r.m.s.-modes will obviously influence the growth of the streak amplitude, which we define at each downstream position as $\max_y(\max_z(\bar{U}) - \min_z(\bar{U}))$. As we consider the mean flow, the modes in frequency–wavenumber space that are associated with the streak amplitude will be $(0, \beta)$, β being any integer. In figure 19(*a–d*) the downstream development of the streak amplitude and the three most important streak modes (0, 2), (0, 4) and (0, 6) are plotted for the five different generation methods. Except for the DAMP case, the (0, 2) mode is dominating. A Fourier expansion of the expression for the DAMP generation (equation (2.7)) reveals that the DAMP method also directly generates modes $(0, 2m)$, with continuously decreasing strength for increasing integer m. This initial generation of (0, 2) is clearly seen at $x = 190$ mm in figure 19(*b*) and is in better agreement with the experiment, which also has a higher streak amplitude at the generation point apart from growing more rapidly downstream. The initial generation of (0, 2) has little effect on its downstream development as the forcing from $(1, \pm 1)$ modes is dominating. A week initial generation of the (0, 4) and (0, 6) modes by the DAMP method can also be observed. Generation by stepwise blowing

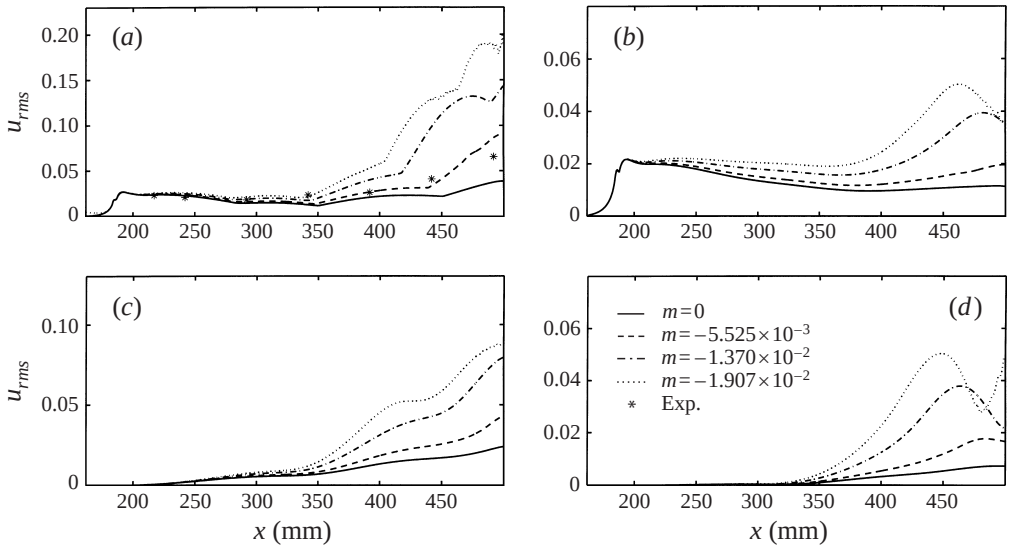

FIGURE 20. (*a*) u_{rms}, (*b*) (1, 1) mode, (*c*) (1, 3) mode and (*d*) (1, 5) mode for simulations with different pressure gradient m and experiment.

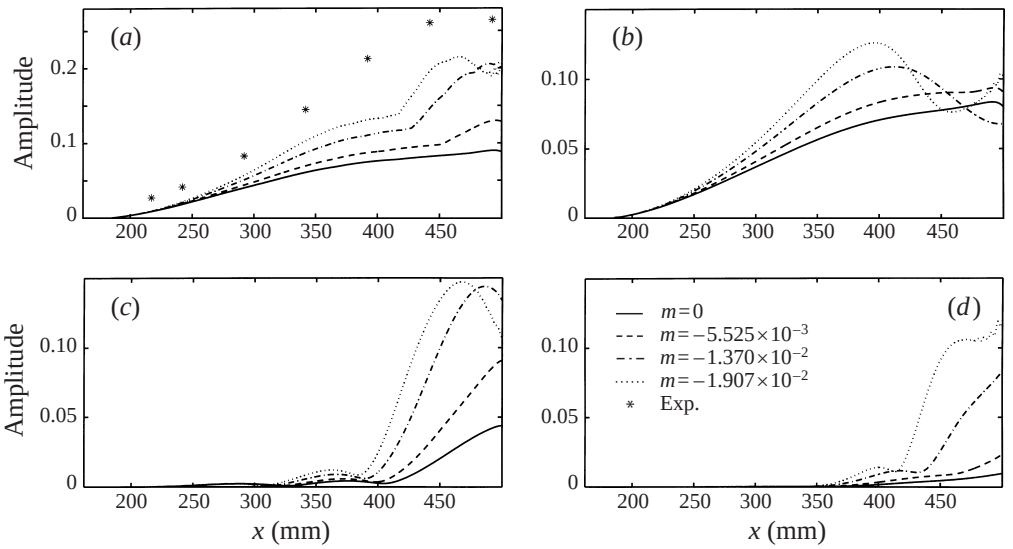

FIGURE 21. (*a*) Streak amplitude, (*b*) (0, 2) mode, (*c*) (0, 4), and (*d*) (0, 6) mode for simulations with different pressure gradient and experiment.

and suction generates the (1, 5) mode initially and the nonlinear interaction of (1, 5) and (1, 1) transfers energy to the (0, 6) mode, which is observed to appear shortly downstream of the generation point for the STEP case in figure 19(*d*).

3.2.2. *Effects of pressure gradient*

The investigation of disturbance generation did not explain the discrepancy in the streak growth observed in figure 19(*a*), something that could be caused by a slight mean pressure gradient in the experiment. We observed that the $(1, \pm1)$ modes decayed faster in the simulations than in the experiment (figure 15) and

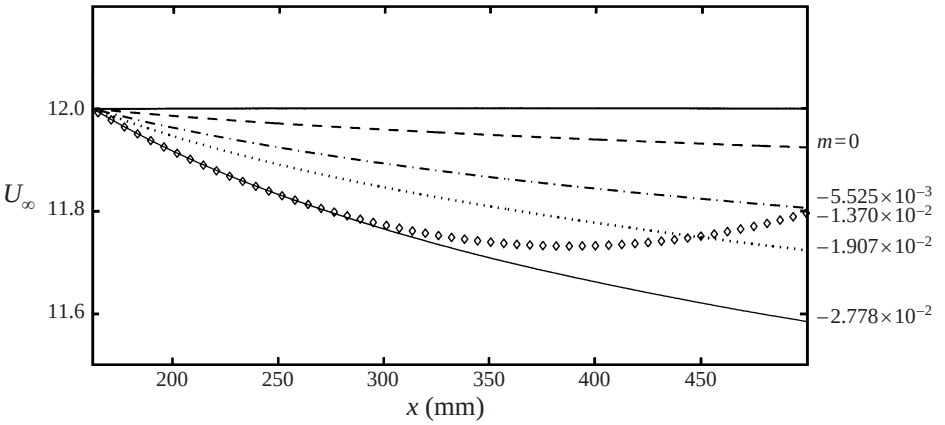

FIGURE 22. Free-stream velocity caused by the pressure gradient used in the detailed modelling ($\diamond$) together with the variation for the five different m exponents.

therefore chose a positive pressure gradient. That will decrease the damping of the oblique waves and thereby increase the forcing of the streaks. Three simulations with Falkner–Scan flow were performed, where the exponent m in equation (2.6) was set to -5.525×10^{-3}, -1.370×10^{-2} and -1.907×10^{-2}. The oblique waves were generated by blowing and suction with a sinusoidal spanwise distribution. Figure 20(*a*) shows the filtered u_{rms} as function of downstream position for the zero-pressure-gradient case and the experiment, together with the three cases with pressure gradient. An increased adverse pressure gradient does indeed decrease the damping of the $(1, 1)$ mode associated with the u_{rms} curve and increase the growth of the higher modes dominating after $x = 350$ mm (figure 20*b,c*). The increased growth of higher modes is caused both by the stronger forcing from the less damped oblique waves and the change of pressure gradient and this is also noted in figure 21(*a–c*) displaying the streak amplitude and the associated modes. Although a faster downstream development is caused by a positive pressure gradient, the qualitative characteristics of the transition scenario are not altered by the pressure gradient. We note that the experimental data for u_{rms} up to $x = 350$ mm agree better with the simulation, having higher positive pressure gradient, and the corresponding curve of streak amplitude also gives the closest agreement, although it is still under-predicted.

3.3. *Detailed modelling*

The results on how the generation method and a pressure gradient influence the transition scenario studied will in this section be used to model the experiment closely. Using blowing and suction is obvious since that was used in the experiment. The good agreement in the u_{rms} between the simulations and the experiment given by the STEP method was shown in figure 18. Moreover, in figure 21(*a*) one observes that the streak amplitude in the experiment starts at a higher level than the curves from the simulations. An increase in initial streak amplitude was observed when the DAMP method was used in figure 19(*a,b*) and consequently a damping factor for suction of 0.7 was used for the results presented in this Section. An adverse pressure gradient was specified to get good agreement between experiment and simulation results for the growth of the $(1, \pm 1)$ modes for the first 150 mm downstream of the generation device. A favourable pressure gradient was used after that in an attempt to avoid early transition. The free-stream velocity variation with downstream location

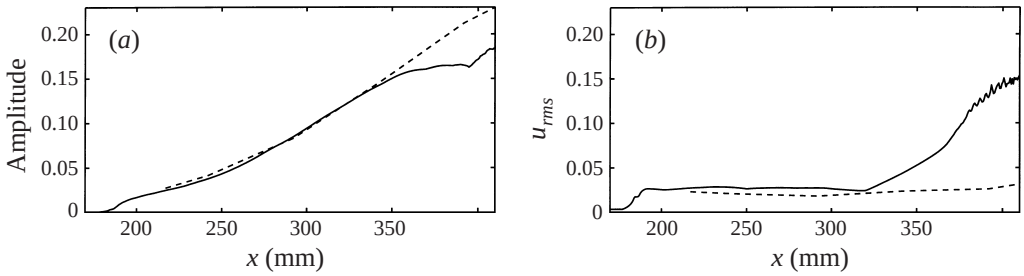

FIGURE 23. (*a*) Streak amplitude and (*b*) u_{rms} of experiment (—) and simulation (- -) with a closely modelled generation mechanism and pressure gradient to match initial u_{rms} development.

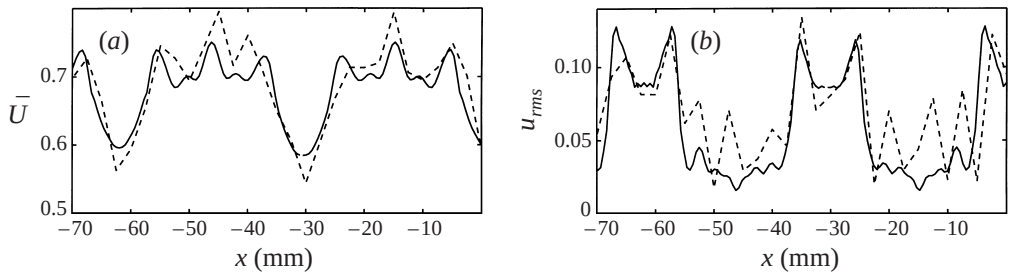

FIGURE 24. Spanwise variation of (*a*) $\bar{U}$ and (*b*) u_{rms} of experiment (—) and simulation (- -) with a closely modelled generation mechanism and pressure gradient to match initial u_{rms} development. Because of the earlier transition in simulation, downstream positions were chosen to get equal maxima of u_{rms}. The downstream positions were $x = 391$ mm in the simulation and $x = 514$ mm in the experiment.

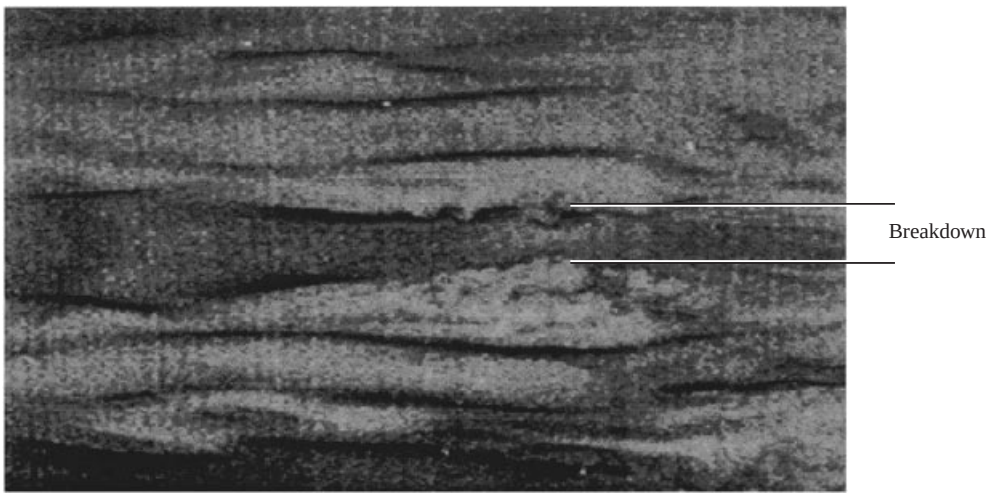

FIGURE 25. Late transition stage from flow visualization of oblique transition. Observe that turbulent high-frequency oscillations are first formed at the spanwise edge of the streaks.

associated with the pressure gradient used is displayed in figure 22, together with the variation of U_∞ for the five different Falkner–Skan profiles used earlier in § 3.2.2. Only a very small pressure gradient was observed in the experiment but other flow characteristics could explain the larger growth rates observed in the experiment.

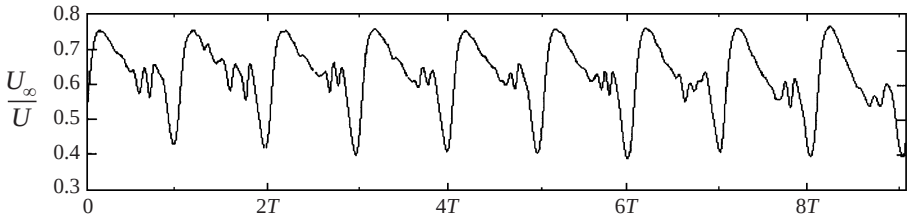

FIGURE 26. Time signal at $z = -2.5$ mm, $x_v = 566$ mm, $y/\delta_r = 1.55$.

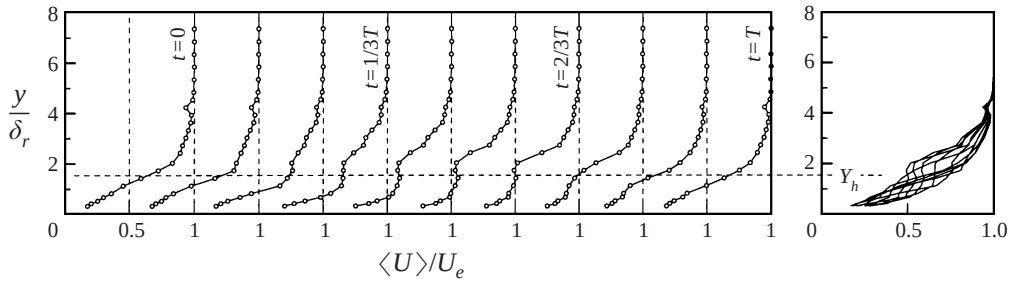

FIGURE 27. Non-stationary phase-averaged mean velocity profiles, $x_v = 566$ mm, $z = -2.5$ mm.

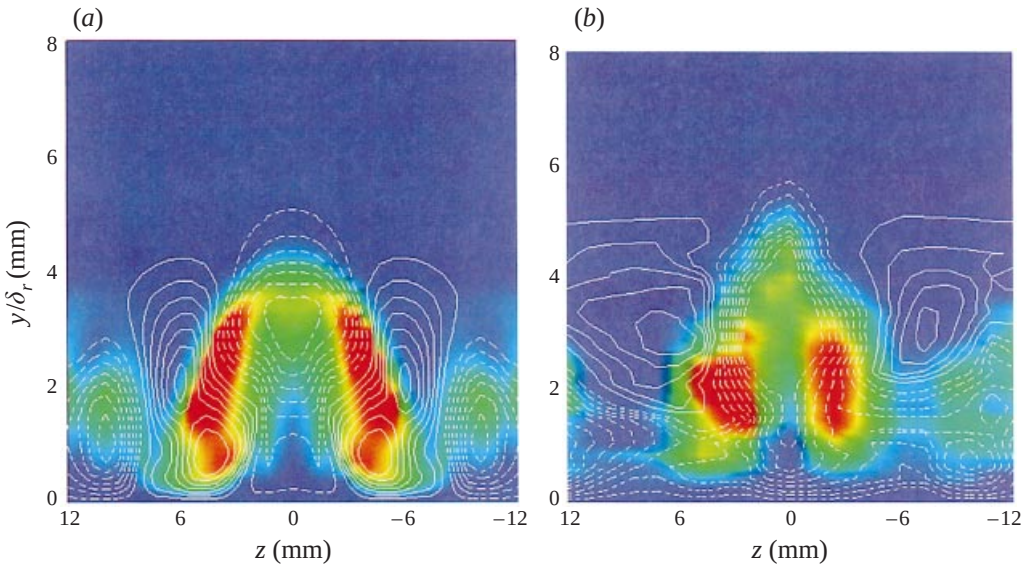

FIGURE 28. u_{rms} represented by colours in a scale from blue-minimum to red-maximum in a plane perpendicular to the flow. White contours represent $\bar{U} - \text{mean}_z(\bar{u})$ solid contours positive values and dashed contours negative values. Simulation data (*a*) are from $x = 410$ mm and the experimental data (*b*) from $x = 566$ mm, as transition is earlier in the simulation.

Klingmann *et al.* (1993) for example concluded in their investigation of the stability of T-S-waves that an unsuitable leading edge often explained high growth rates observed in experiments.

Figure 23 displays the downstream variation of u_{rms} and the streak amplitude for both the experiment and a simulation using the above described detailed modelling.

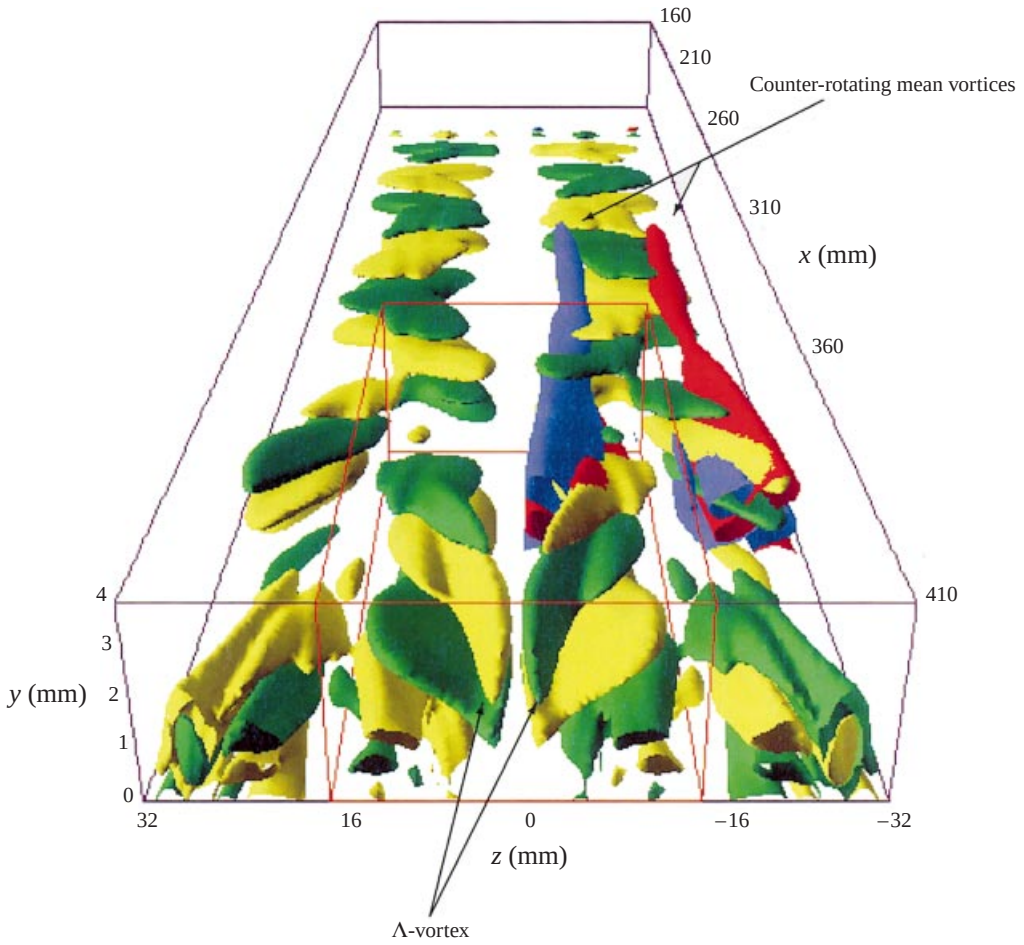

FIGURE 29. Isosurfaces of positive and negative instantaneous streamwise vorticity from the simulation are coloured yellow and green respectively. Note the formation of a Λ-vortex in the downstream part of the box. A pair of counter-rotating vortices is displayed as red and blue surfaces representing positive and negative mean of streamwise vorticity, respectively.

The agreement is excellent to $x = 320\,\text{mm}$ for u_{rms} and to $x = 340\,\text{mm}$ for the streak amplitude. Further downstream the pressure gradient cause earlier transition in the simulation. Therefore the later stages of the breakdown process occur at earlier streamwise positions than in the experiment. Thus a comparison of features from a particular stage in the transition process will have to occur at different streamwise positions in experiment and simulation. In figure 24 the spanwise variation of u_{rms} and $\bar{U}$ are compared at downstream positions where the transition process has reached the same stage, i.e. where the maximum of u_{rms} is the same in both simulation and experiment. The mean and r.m.s. values at $x = 391\,\text{mm}$ in the simulation are compared with the corresponding values at $x = 514\,\text{mm}$ in the experiment. The agreement shown requires that the amplitude and phase of all modes involved have the correct relations and is achieved thanks to the good modelling of the generation device for oblique waves. The difference in streak amplitude in figure 24(*a*) is smaller than that observed in figure 21(*a*). The reason for this is that the streak amplitude in the experiment decays after $x = 467\,\text{mm}$ (figure 10*b*).

3.4. *Final breakdown*

3.4.1. *The onset of high-frequency fluctuations*

The last figure (figure 24) of the previous subsection shows that the peaks of u_{rms} appear where the spanwise gradient of $\bar{U}$ has its maximum. This is different from the early stages of oblique transition where u_{rms} is dominated by the oblique waves and therefore lies in the middle of the low-speed streaks (cf. figure 7). The meandering streaks displayed in the flow visualization (figure 6) indicate that large u_{rms} values are produced, as the boundary between high- and low-speed fluid oscillates in the spanwise direction. A close-up of the streaks in the flow visualization also displays the first turbulent high-frequency oscillations just where the colour of the smoke pattern changes from black to white (figure 25).

The distribution of u_{rms} in a plane perpendicular to the flow is presented in colour scale for both simulation and experiment in figure 28(*a,b*) below. The experimental data are taken from $x = 566\,\text{mm}$ and the simulation results at $x = 410\,\text{mm}$, a difference that again is attributed to the earlier transition in the simulation. A characteristic symmetric structure with two legs, each containing a maximum of u_{rms}, joined at their upper half is identified in both figures. The figures also include contours of $\bar{U} - \text{mean}_z(\bar{U})$ and the shear is found to be high in regions close to where the maxima of u_{rms} are situated. This is an indication that it is oscillations of high instantaneous spanwise shear between the streaks that causes the high u_{rms} values. The wall-normal and spanwise positions, where the peaks of u_{rms} are found, are the same as those where the first appearance of high-frequency oscillations was detected by a hot wire. A time trace from the experiment at such a position is presented in figure 26, where each fundamental cycle contains high-frequency oscillations. A spectral analysis reveals both high amplitude of several subharmonics and a range of amplified frequencies at approximately 800 Hz. In the phase-averaged streamwise velocity profiles collected at different phases during a fundamental time period in the experimental investigation (figure 27), we find inflectional profiles. The positions of inflectional profiles coincide with the positions where we found the peaks of u_{rms} and the high-frequency oscillations. The inflectional profiles were only present during part of a time period and the same was true for the high-frequency oscillations.

3.4.2. *Flow structures*

It is interesting to relate the statistical quantities and the instantaneous observations discussed above to structures appearing in the flow during transition. In figure 29 positive and negative isosurfaces of instantaneous streamwise vorticity are displayed in yellow and green respectively. At $x = 200\,\text{mm}$ a spanwise row of small surfaces is revealed where the wave generator is situated. The oblique waves are then seen as streamwise rows of alternating positive and negative vorticity. When the flow evolves downstream the patches of vorticity are gradually divided ($x = 360\,\text{mm}$). Groups of three surfaces overlapping each other are separated alternately to the left and to the right. Two such groups, of three surfaces, from neighbouring rows form new groups, in which we can identify the middle pair of surfaces as counter-rotating vortices forming a Λ-shaped structure. The two pairs of surfaces above and below do not represent vortices but regions of high wall-normal shear of the spanwise velocity, $\partial w/\partial y$. Observe that there is no spanwise vortex connecting the legs of the Λ-vortex, which is natural since the legs have developed independently and thereafter been drawn towards each other. The red and blue surfaces in figure 29 represent positive and negative mean streamwise vorticity. It is that motion that creates the low- and

Investigator	$R_{\delta*}$	u^0_{rms}	F	$\beta^0_{\delta^*}$
Joslin *et al.* (1993)	900	0.02, 0.002	86	0.20
Berlin *et al.* (1994)	400	0.02	200	0.19
Wiegel (1996)	664	0.023	59	0.083
Present	664	0.023	59	0.083
Elofsson (1998)	583	0.075, 0.05	43	0.13

TABLE 3. The main parameter settings used in investigations of oblique transition in zero-pressure-gradient boundary layers. Some results with other settings are also included in most investigations. $R_{\delta*}$ represents the Reynolds number based on the displacement thickness, F the non-dimensional frequency and $\beta^0_{\delta^*}$ the spanwise wavenumber at the generation position non-dimensionalized by the displacement thickness. u^0_{rms} is taken as the maximum u_{rms} measured at the inflow position or at the first measurement station downstream of the disturbance generation device. Two amplitudes were used in the first and last investigations in the table.

high-speed streaks in the streamwise velocity and it is also responsible for the observed splitting of the instantaneous vorticity patches. In the first portion of the box the red and blue structures are mainly what we previously have called the $(0, 2)$ mode and the yellow and green structures correspond to the $(1, \pm 1)$ mode. In the downstream region of the box the mean streamwise vorticity surfaces instead tend to be a trace of the instantaneous vorticity structures.

In figure 30 the structure inside the smaller red box in figure 29 is studied. The green and yellow surfaces are the same in figures 29 and 30 and in figure 30(*a*) the red and blue surfaces represent positive and negative wall-normal disturbance velocity respectively. By disturbance velocity we mean that the laminar velocity has been subtracted. The original checked pattern of positive and negative wall-normal velocity disturbances has here been deformed by the Λ-vortex. It has strengthened the upwash in the middle of the structure, which creates the strong shear layer observed in figure 30(*b*). In that figure the red surfaces represent the wall-normal shear of the streamwise disturbance velocity. One observes both a high shear layer riding on top of the Λ-vortex and strong shear layers underneath the Λ-vortex. The lower shear layers start at the wall and follow the Λ-vortex upwards. They are caused by fluid with high streamwise velocity brought down by the negative wall-normal velocity (blue surfaces in figure 30*a*). In figure 30(*c*) the Λ-vortex has been cut and inside it, surfaces of minimal wall-normal shear of the streamwise velocity are displayed. That $\partial u/\partial y$ has a local minimum means that there is a inflectional velocity profile at that position. The isocurves at the face of the box in figure 30(*c*) represents constant u_{rms} in that plane. The results are consistent with the experimental results showing the highest u_{rms} values in the region where we find the inflectional profiles.

4. Discussion

4.1. *Comparison with previous investigations of oblique transition*

The qualitative agreement between other investigations of oblique transition in incompressible boundary layers and the present investigation is good. Most characteristic is the initial rapid growth of the $(0, 2)$ streak mode caused by non-modal mechanisms. A detailed comparison is difficult to make as the parameters used differ considerably as can be seen in table 3. The relations between the modes presented by Joslin *et al.* (1993) agree well with both those presented by Berlin *et al.* (1994) and those found in

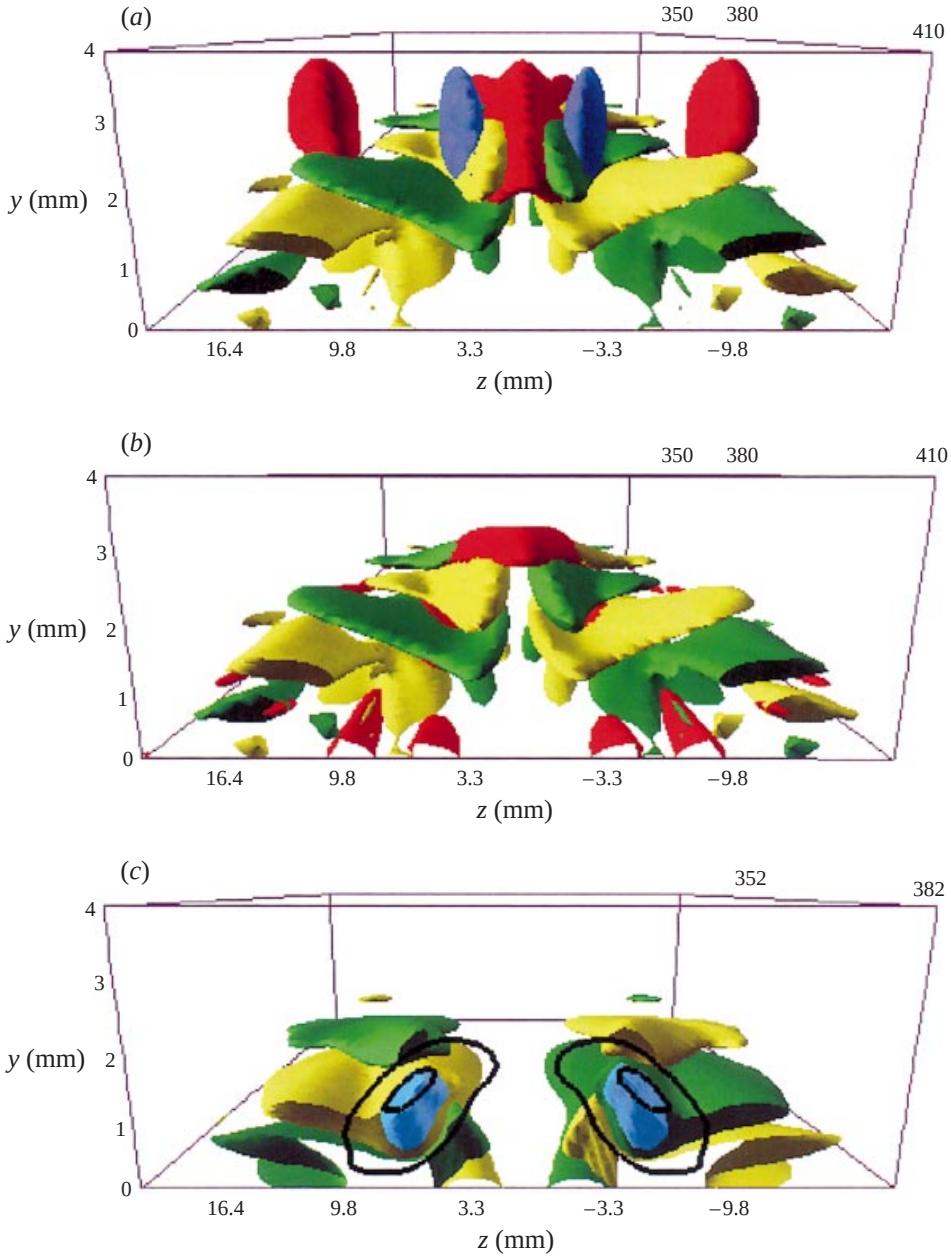

FIGURE 30. Isosurfaces of positive and negative instantaneous streamwise vorticity are coloured yellow and green respectively. In (*a*) the red and blue surfaces represents constant positive and negative values of the wall-normal disturbance velocity respectively. In (*b*) and (*c*) the red and blue surfaces represent constant positive and negative values respectively of the wall-normal shear of the streamwise disturbance velocity, isolines are constant u_{rms}.

the present investigation. The structures we have identified in the late transition state were in a re-examination also found in the data of Berlin *et al.* (1994), and Elofsson (1998) also observed Λ-shaped structures in a staggered pattern. The development of Fourier components in Elofsson (1998) displays two features that differ from the

standard calculations. One is the high values of the $(0,4)$ mode, which is explained by the fact that he used a blowing and suction technique similar to that used in the present investigation. We have shown that it is well modelled in the numerics by the DAMP generation method, which also produced the $(0,4)$ mode. The second difference is the low level of the $(1,3)$ mode. That is more difficult to explain as one would expect it to be generated by the nonlinear interaction of the strong $(1,\pm1)$ and $(0,2)$ modes as in other experiments and calculations.

4.2. *Relation to transition caused by streamwise vortices and free-stream turbulence*

Strong growth of streamwise streaks with the same wall-normal mode shape as in the present investigation has also been observed in experiments on boundary layers subjected to free-stream turbulence (Klebanoff 1971; Kendall 1985; Westin *et al.* 1994). Bertolotti & Kendall (1997) introduced a single free-stream vortex in an experiment and found the same boundary layer response as to free-stream turbulence. They compared the boundary layer response to a receptivity model proposed by Bertolotti (1997), which did not include the leading edge, and found good agreement. After matching the strength of the boundary layer response of the experiment, they calculated the downstream streak growth using linear PSE and found good agreement with the experiment. Berlin & Henningson (1999) introduced both streamwise streaks and oblique waves in the free stream in a numerical investigation and both types of disturbance caused streak growth in the boundary layer. They identified both a linear and a nonlinear receptivity mechanism.

As in the present study the observed streak growth in all these investigations agrees well with the theory of non-modal growth. Moreover, Andersson *et al.* (1997) found good agreement with the experimental results by Westin *et al.* (1994) when they investigated spatial non-modal growth.

4.3. *Similarities with the structures of K-type and H-type transition*

The structures that we have identified in the late stage of oblique transition have many similarities with those previous investigators have found in the corresponding stage of K- and H-type transition. We find for example Λ-vortices with the strong shear layers on top, streamwise vortices deforming the mean flow and inflectional profiles. Structures are easier to extract from numerical simulations and comparisons can be made with the spatial simulation of K-type transition by Rist & Fasel (1995) or the temporal simulations of both K- and H-type transition by Laurien & Kleiser (1989). Detailed flow structures of both K-type and H-type transition are also reported for channel flow by Krist & Zang (1986), Zang & Krist (1989) and others. Experimental investigators reporting details of the flow structures before breakdown are for example Williams, Fasel & Hama (1984) for K-type and Corke & Mangano (1989) for H-type transition.

It is important to note that we are discussing three different transition scenarios. The differences lie in the initial conditions and the initial mechanisms for disturbance growth. Oblique transition does not need two-dimensional TS-waves, which are essential for the secondary instability scenarios, K-type and H-type transition. Oblique transition instead is caused by nonlinear interactions and non-modal growth mechanisms. However, by studying the initial conditions and the vital nonlinearly generated modes in the three scenarios we can understand that the striking similarities found in the late transition stage are in all three cases caused by oblique waves interacting with streamwise vortices.

The initial conditions of the important modes for the three transition scenarios

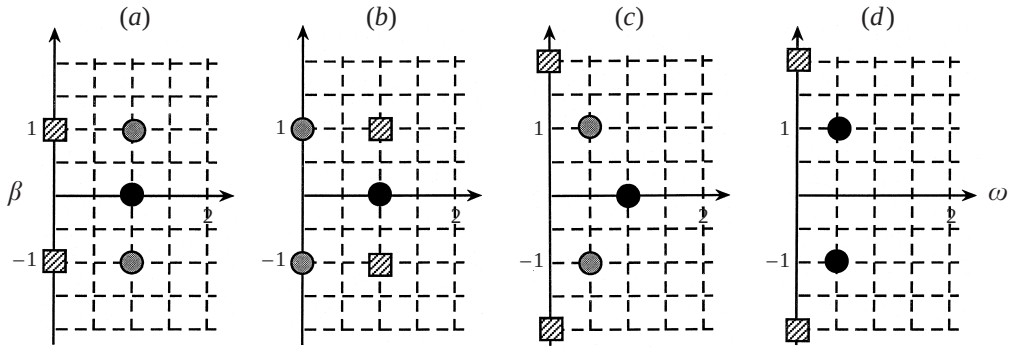

FIGURE 31. Graphs displaying the relation between the most important modes in (*a,b*) K-type, (*c*) H-type and (*d*) oblique transition. Modes marked with black dots are initiated with the largest amount of energy. Grey dots symbolize modes initiated with a small amount of energy and squares represent modes that are generated nonlinearly and are vital in the transition process or for what is observed at the late stage of transition.

are indicated in figure 31(*a–d*) together with some important nonlinearly generated modes. Black dots mark the modes where the largest initial energy is introduced in the flow. Grey dots mark modes that are initiated with a smaller amount of energy and finally squares represent vital modes that are generated nonlinearly from the initially exited modes. Figure 31(*a,b*) represents the K-type scenarios with the main initial energy in the $(1,0)$ mode. In 31(*a*) the oblique modes $(1,\pm1)$ are also initiated as is done in many numerical simulations. The counter-rotating vortices with associated streaks $(0,\pm1)$ that causes the spanwise modulation of the flow are in this case generated nonlinearly. In experiments it is usual to initiate the vortices/streaks and the TS-wave and let the oblique modes be generated nonlinearly, which is illustrated in figure 31(*b*). The $(1,\pm1)$ modes in figure 31(*a,b*) also generate the $(0,\pm2)$ modes, but with a small amplitude compared to the interaction of $(1,0)$, $(1,\pm1)$ and $(0,1)$. Even so the $(0,\pm2)$ modes can grow to an amplitude comparable to that of the $(0,\pm1)$ ones, as it does at the late stages in the computations by Laurien & Kleiser (1989). The initial conditions for H-type transition are described in figure 31(*c*), with the main initial energy still in the $(1,0)$ mode and with a small amount in the oblique subharmonic $(1/2,\pm1)$ modes. The vortex-streak modes of importance now are $(0,\pm2)$, which are nonlinearly generated by the subharmonic modes. Finally oblique transition is described in figure 31(*d*). The two-dimensional TS-mode $(1,0)$ is excluded and the initial energy is instead only introduced in the oblique waves $(1/2,\pm1)$. The vortex-streak modes $(0,\pm2)$ are generated nonlinearly exactly as in H-type transition, but the energy in the oblique waves is higher and consequently the forcing of the vortex-streak mode stronger. Therefore the streaks are captured in a flow visualization rather than the Λ-vortices as for H-type transition. The naming of modes is of course just a matter of normalization and in an attempt to simplify the comparison, oblique transition in this discussion involve modes $(0,\pm2)$ and $(1/2,\pm1)$, whereas we previously have called these modes $(0,\pm2)$ and $(1,\pm1)$.

With the sketches in figure 32 we illustrate the late stages of the three transition scenarios. The flow is from left to right and the grey shading represents the wall-normal velocity of oblique waves, dark for positive and bright for negative. The circles with arrows symbolize streamwise elongated counter-rotating vortices, with the rotation direction indicated by the arrows. Contours of the wall-normal velocity

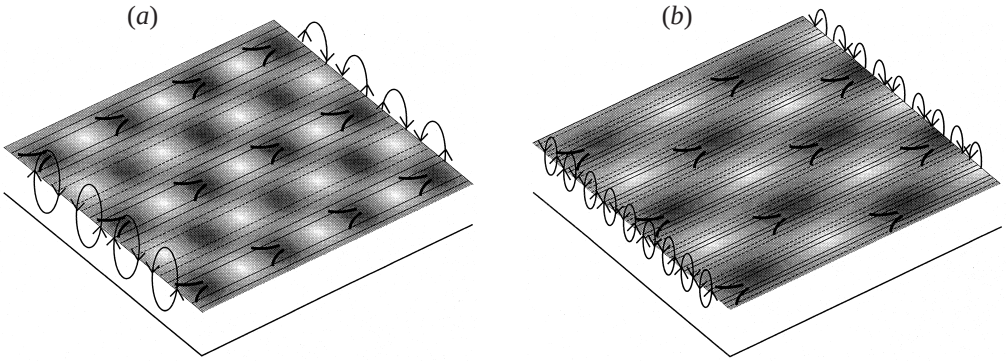

FIGURE 32. Relation between oblique waves, Λ-vortices and streamwise vortices for (*a*) K-type transition and (*b*) H-type transition and oblique transition. The wall-normal velocity components of the oblique waves are represented by the grey scale pattern, where dark means positive and bright negative velocity. The arrows on the circles indicate the rotation direction of counter-rotating streamwise vortices. Solid and dashed lines are contours of the wall-normal velocity associated with the vortices. Positions where Λ-vortices appear are marked by the black Λ symbols.

associated with the vortices are also included in the figures. Solid contours indicate positive and dashed negative wall-normal velocity. The wall-normal motion will create streaks with low and high streamwise velocity, appearing where the solid and dashed contours are respectively. In 32(*a*) the streamwise and spanwise scales of the oblique waves are the same and the spanwise wavelength of the vortex pattern is the same as that of the oblique waves. These conditions correspond to K-type transition also shown in figure 31(*a,b*). Λ-vortices will appear at positions where the oblique waves produce a maximal wall-normal velocity *and* the vortices produce positive wall-normal velocity. Aligned black lambdas mark where these conditions are met. The conditions shown in figure 32 correspond to oblique and H-type transition, with twice the streamwise scale of the oblique waves compared to K-type transition and the spanwise wavelength of the vortices halved (cf. figure 31*c,d*). The staggered Λ-vortices are marked using the same criteria as in figure 32(*a*). Note that the appearing patterns of Λ-vortices in the three transition scenarios can be inferred without the use of any TS-waves. In oblique transition the present TS-wave ((2, 0) mode) has low amplitude. In calculations of the other scenarios by Laurien & Kleiser (1989) and Krist & Zang (1986) we find that the amplitude of the TS-wave is below those of the oblique waves and the streamwise vortices at the late transition state. PIV measurements of the instantaneous streamwise velocity from the three transition scenarios are compared in figure 33. Both streaks and Λ-shapes can be observed in all three figures but the amplitude relation between them differs.

5. Conclusions

We have performed both physical experiments and numerical simulations of oblique transition, a transition scenario initiated by two oblique waves only. In this first experiment on oblique transition in an incompressible boundary layer, blowing and suction was used to generate the oblique waves. Hot-wire measurements as well as flow visualizations with a laser technique were used to analyse the physical flow. The experiment verified earlier computational and theoretical results. The nonlinear interaction of the oblique waves generates streamwise vortices. The lift-up mecha-

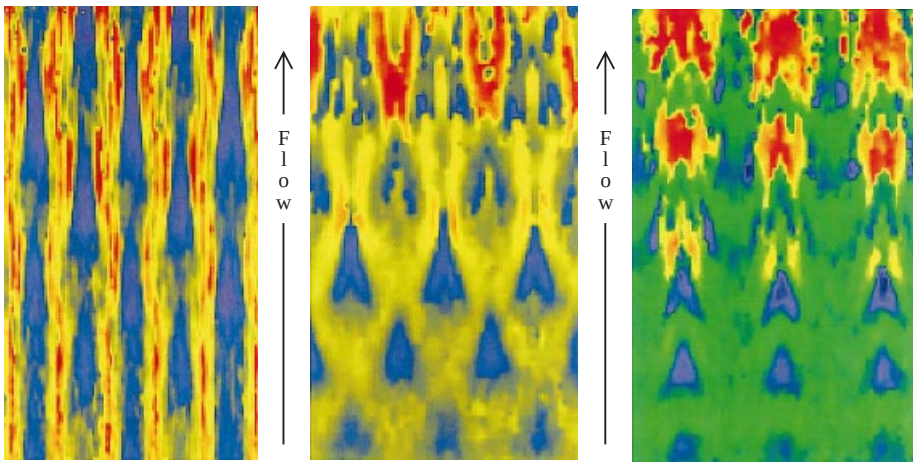

FIGURE 33. The instantaneous streamwise velocity from three transition scenarios measured with the PIV technique. From left to right: oblique transition, H-type transition and K-type transition. The flow direction is from the bottom to top of the figures. Both Λ-shapes and streaks can be observed in all three scenarios.

nism associated with the vortices causes spanwise variation of the mean flow with alternating high- and low-streamwise velocity streaks. The streaks grow downstream in a manner consistent with the theories on non-modal growth. Efforts were made to closely model the experiment in the numerical code and five different methods for disturbance generation were compared. They all produced qualitatively similar transition scenarios but important differences were also found. The closest agreement with the disturbance generated by the experimental device was found when we used a blowing and suction technique, where the amplitude of the wall-normal velocity changed stepwise in the spanwise direction and the suction amplitude was 70% of the blowing amplitude. The effect of a positive pressure gradient was also investigated numerically and was found to move all stages of the transition scenario upstream. Imposing a positive pressure gradient in the simulation decreased the initial damping of oblique waves to better correspond to the experimental development. This resulted in a faster growth of the streak amplitude, which was also in agreement with the experiment, but the computed flow was in this case found to reach a turbulent stage upstream of the corresponding stage in the experiment. At the late stages of transition we identified high shear layers riding on top of vortex pairs forming the legs of Λ-shaped structures. The positions of the Λ-shaped vortex pairs coincided with the appearance of u_{rms} peaks as well as high-frequency oscillations in the experimental time traces. The flow structures observed in the late stage of transition were very similar to those reported by both numerical and experimental investigators of K- and H-type transition. These similarities are explained by the common feature of all three transition scenarios, namely oblique waves and streamwise vortices.

The authors greatly acknowledge the contributions of all colleagues inspiring this work with discussions, especially Peter Schmid for calculating the maximum resonance for Blasius boundary layers. We also wish to thank the technical staff at DLR for the assistance during the experiments. The computational par of this work has been supported by TFR (Swedish Research Council for Engineering Sciences).

REFERENCES

Andersson, P., Berggren, M. & Henningson, D. 1997 Optimal disturbances in boundary layers. In *Progress in Systems Control*. Birkhäuser.

Andersson, P., Berggren, M. & Henningson, D. 1999 Optimal disturbances and bypass transition in boundary layers. *Phys. Fluids*. **11**, 134–150.

Berlin, S. & Henningson, D. S. 1999 A nonlinear mechanism for receptivity of free-stream disturbances. *Phys. Fluids* (to appear).

Berlin, S., Lundbladh, A. & Henningson, D. S. 1994 Spatial simulations of oblique transition. *Phys. Fluids* **6**, 1949–1951.

Bertolotti, F. P. 1997 Response of the blasius boundary layer to free-stream vorticity. *Phys. Fluids* **9**, 2286–2299.

Bertolotti, F. P., Herbert, T. & Spalart, P. R. 1992 Linear and nonlinear stability of the Blasius boundary layer. *J. Fluid Mech.* **242**, 441–474.

Bertolotti, F. P. & Kendall, J. M. 1997 Response of the blasius boundary-layer to controlled free-stream vortices of axial form. *AIAA Paper* 97-2018.

Butler, K. M. & Farrell, B. F. 1992 Three-dimensional optimal perturbations in viscous shear flow. *Phys. Fluids* A **4**, 1637–1650.

Chang, C.-L. & Malik, M. R. 1992 Oblique-mode breakdown and secondary instability in a supersonic boundary layers using nonlinear pse. In *Instability, Transition and Turbulence* (ed. M. Y. Hussaini, A. Kumar & C. L. Streett), pp. 231–241. Springer.

Chang, C.-L. & Malik, M. R. 1994 Oblique-mode breakdown and secondary instability in supersonic boundary layers. *J. Fluid Mech.* **273**, 323–360.

Corke, T. C. & Mangano, R. A. 1989 Resonant growth of three-dimensional modes in transitional Blasius boundary layers. *J. Fluid Mech.* **209**, 93–150.

Ellingsen, T. & Palm, E. 1975 Stability of linear flow. *Phys. Fluids* **18**, 487–488.

Elofsson, P. A. 1998 Experiment on oblique transition in wall bounded shear flows. PhD thesis, Royal Institute of Technology, Stockholm, Sweden.

Elofsson, P. A. & Alfredsson, P. H. 1998 An experimental study of oblique transition in plane poiseuille flow. *J. Fluid Mech.* **358**, 177–202.

Elofsson, P. A. & Lundbladh, A. 1994 Ribbon induced oblique transition in plane poiseulle flow. In *Bypass Transition – Proceedings from a Mini-Workshop* (ed. D. S. Henningson), pp. 29–41. *TRITA-MEK Tech. Rep.* 1994 : 14. Royal Institute of Technology, Stockholm, Sweden.

Fasel, H. & Konzelmann, U. 1990 Non-parallel stability of a flat-plate boundary layer using the complete navier-stokes equations. *J. Fluid Mech.* **221**, 311–347.

Fasel, H. & Thumm, A. 1991 Direct numerical simulation of three-dimensional breakdown in supersonic boundary layer transition. *Bull. Am. Phys. Soc.* **36**, 2701.

Fasel, H., Thumm, A. & Bestek, H. 1993 Direct numerical simulation of transition in supersonic boundary layers: Oblique breakdown. In *Transitional and Turbulent Compressible Flows* (ed. L. Kral & T. Zang). ASME FED, Vol. 151, pp. 77–92.

Gustavsson, L. H. 1991 Energy growth of three-dimensional disturbances in plane Poiseuille flow. *J. Fluid Mech.* **224**, 241–260.

Hanifi, A. & Henningson, D. S. 1998 The compressible inviscid algebraic instability for streamwise independent disturbances. *Phys. Fluids* **10**, 1784–1786.

Hanifi, A., Schmid, P. J. & Henningson, D. S. 1996 Transient growth in compressible boundary layer flow. *Phys. Fluids* **8**, 51–65.

Henningson, D. S. 1996 Comment on "Transition in shear flows. Nonlinear normality versus non-normal linearity" [phys. fluids 7 3060 (1995)]. *Phys. Fluids* **8**, 2257–2258.

Henningson, D. S., Lundbladh, A. & Johansson, A. V. 1993 A mechanism for bypass transition from localized disturbances in wall bounded shear flows. *J. Fluid Mech.* **250**, 169–207.

Herbert, T. 1983*a* Secondary instability of plane channel flow to subharmonic three-dimensional disturbances. *Phys. Fluids* **26**, 871–874.

Herbert, T. 1983*b* Subharmonic three-dimensional disturbances in unstable shear flows. *AIAA Paper* 83-1759.

Herbert, T. 1988 Secondary instability of boundary layers. *Ann. Rev. Fluid Mech.* **20**, 487–526.

Joseph, D. D. 1976 *Stability of Fluid Motions I*. Springer.

Joslin, R. D., Streett, C. L. & Chang, C. L. 1992 Oblique wave breakdown in an incompress-

ible boundary layer computed by spatial dns and pse theory. In *Instability, Transition and Turbulence* (ed. M. Y. Hussaini, A. Kumar & C. L. Streett), pp. 304–310. Springer.

Joslin, R. D., Streett, C. L. & Chang, C. L. 1993 Spatial direct numerical simulations of boundary-layer transition mechanisms: Validation of PSE theory. *Theor. Comput. Fluid Dyn.* **4**, 271–288.

Kachanov, Y. S. 1994 Physical mechanisms of laminar-boundary-layer transition. *Ann. Rev. Fluid Mech.* **26**, 411–482.

Kachanov, Y. S., Kozlov, V. & Levchenko, V. Y. 1977 Nonlinear development of a wave in a boundary layer. *Izv. Akad. Nauk SSSR, Mekh. Zhidk. Gaza* **3**, 49–53 (in Russian).

Kelvin, Lord 1887 Stability of fluid motion – rectilinear motion of a viscous fluid between two parallel planes. *Phil. Mag.* **24**, 188–196.

Kendall, J. M. 1985 Experimental study of disturbances produced in a pre-transitional laminar boundary layer by weak freestream turbulence. *AIAA Paper* 85-1695.

Kim, J., Moin, P. & Moser, R. 1987 Turbulence statistics in fully developed channel flow. *J. Fluid Mech.* **177**, 133–166.

Klebanoff, P. S. 1971 Effect of freestream turbulence on the laminar boundary layer. *Bull. Am. Phys. Soc.* **10**, 1323.

Klebanoff, P. S., Tidstrom, K. D. & Sargent, L. M. 1962 The three-dimensional nature of boundary layer instability. *J. Fluid Mech.* **12**, 1–34.

Kleiser, L. & Zang, T. A. 1991 Numerical simulation of transition in wall-bounded shear flows. *Ann. Rev. Fluid Mech.* **23**, 495–537.

Klingmann, B. G. B., Boiko, A., Westin, K., Kozlov, V. & Alfredsson, P. 1993 Experiments on the stability of Tollmien–Schlichting waves. *Eur. J. Mech.* B/*Fluids* **12**, 493–514.

Kreiss, G., Lundbladh, A. & Henningson, D. S. 1994 Bounds for threshold amplitudes in subcritical shear flows. *J. Fluid Mech.* **270**, 175–198.

Krist, S. E. & Zang, T. A. 1986 Numerical simulation of boundary layers: Part 1. Weak formulation and numerical method. *NASA TM* 88222.

Landahl, M. T. 1975 Wave breakdown and turbulence. *SIAM J. Appl. Maths* **28**, 735–756.

Laurien, E. & Kleiser, L. 1989 Numerical simulation of boundary-layer transition and transition control. *J. Fluid Mech.* **199**, 403–440.

Lu, Q. & Henningson, D. S. 1990 Subcritical transition in plane Poiseuille flow. *Bull. Am. Phys. Soc.* **35**, 2288.

Luchini, P. 1996 Reynolds number independent instability of the Blasius boundary layer over a flat surface. *J. Fluid Mech.* **327**, 101–115.

Lundbladh, A., Henningson, D. S. & Johansson, A. V. 1992 An efficient spectral integration method for the solution of the Navier–Stokes equations. *FFA-TN* 1992-28. Aeronautical Research Institute of Sweden, Bromma.

Lundbladh, A., Schmid, P. J., Berlin, S. & Henningson, D. S. 1994 Simulation of bypass transition in spatially evolving flows. *Proc. AGARD Symp. on Application of Direct and Large Eddy Simulation to Transition and Turbulence, AGARD-CP*-551.

Malik, M. R., Zang, T. A. & Hussaini, M. Y. 1985 A spectral collocation method for the Navier–Stokes equations. *J. Comput. Phys.* **61**, 64–88.

Morkovin, M. V. 1969 The many faces of transition. In *Viscous Drag Reduction* (ed. C. S. Wells). Plenum.

Orr, W. M. F. 1907 The stability or instability of the steady motions of a perfect liquid and of a viscous liquid. Part I: A perfect liquid. Part II: A viscous liquid. *Proc. R. Irish Acad.* A **27**, 9–138.

Reddy, S. C. & Henningson, D. S. 1993 Energy growth in viscous channel flows. *J. Fluid Mech.* **252**, 209–238.

Reddy, S. C., Schmid, P. J., Bagget, P. & Henningson, D. S. 1998 On stability of streamwise streaks and transition thresholds in plane channel flows. *J. Fluid Mech.* **365**, 269–303.

Rist, U. & Fasel, H. 1995 Direct numerical simulation of controlled transition in a flat-plate boundary layer. *J. Fluid Mech.* **298**, 211–248.

Rotta, J. C. 1971 Fortran 4-rechenprogramm für grenzschichten bei kompressiblen ebenen und achsensymmetrische strömungen. *Tech. Rep.* DFVLR-FB 71-51. Institute for Theoretical Fluid Mechanics, Göttingen.

Sandham, N. D., Adams, N. A. & Kleiser, L. 1994 Direct simulation of breakdown to turbulence

following oblique instability waves in a supersonic boundary layer. *First ERCOFTAC Workshop on Direct and Large Eddy Simulation, Guildford, England, March 28–30.*

Schmid, P. J. & Henningson, D. S. 1992. Channel flow transition induced by a pair of oblique waves. In *Instability, Transition and Turbulence* (ed. M. Y. Hussaini, A. Kumar & C. L. Streett), pp. 356–366. Springer.

Schmid, P. J., Reddy, S. C. & Henningson, D. S. 1996 Transition thresholds in boundary layer and channel flow. In *Advances in Turbulence VI* (ed. S. Gavrilakis, L. Machiels & P. A. Monkewitz), pp. 381–384. Kluwer.

Trefethen, L. N. 1997 Psuedospectra of linear operators. *SIAM Rev.* **39**, 383–406.

Trefethen, L. N., Trefethen, A. E., Reddy, S. C. & Driscoll, T. A. 1993 Hydrodynamic stability without eigenvalues. *Science* **261**, 578–584.

Westin, K. J. A., Boiko, A. V., Klingmann, B. G. B., Kozlov, V. V. & Alfredsson, P. H. 1994 Experiments in a boundary layer subject to free-stream turbulence. Part 1. Boundary layer structure and receptivity. *J. Fluid Mech.* **281**, 193–218.

Wiegel, M. 1996 Experimentelle Untersuchung von kontrolliert angeregten dreidimensionalen Wellen in einer Blasius-Grenzschicht. PhD thesis, Der Fakultät für Maschinenwesen der Universität Hannover, Hannover (Germany). Also available as *VDI Fortschritt-Bericht Reihe* 7, vol. 312, 1997.

Williams, D. R., Fasel, H. & Hama, F. R. 1984 Experimental determination of the three-dimensional vorticity field in the boundary-layer transition process. *J. Fluid Mech.* **149**, 179–203.

Zang, T. A. & Krist, S. E. 1989 Numerical experiments on stability and transition in plane channel flow. *Theor. Comput. Fluid Dyn.* **1**, 41–64.